

1 **Robust Imaging of Fault Slip Rates in the Walker Lane and Western Great Basin**
2 **from GPS Data Using a Multi-Block Approach**

7 William C. Hammond¹, Corné Kreemer^{1,2}, Geoffrey Blewitt¹
8
9
10
11

12 1) Nevada Geodetic Laboratory
13 Nevada Bureau of Mines and Geology

14
15 2) Nevada Seismological Laboratory
16 University of Nevada, Reno
17 Reno NV 89557

18
19 *whammond@unr.edu*

20
21
22 Submitted Draft October 2023

23
24
25
26 Key Points:

- 27
28 1. We estimate Walker Lane fault slip rates using a dense geodetic velocity field and a robust
29 multi-block approach
- 30 2. The geodetic estimates are independent of geologic slip rates, but 80% agree with them to
31 within uncertainties
- 32 3. The method images off-fault deformation and vertical axis rotations providing more insight
33 into how crustal motion drives earthquakes

34

35 **Abstract**

36
37 The Walker Lane (WL) in the western Great Basin (GB) is an active plate boundary system
38 accommodating 10-20% of the relative tectonic motion between the Pacific and North American
39 plates. Its neotectonic framework is structurally complex, having hundreds of faults with various
40 strikes, rakes, and crustal blocks with vertical axis rotation. Faults slip rates are key parameters
41 needed to quantify seismic hazard in such tectonically active plate boundaries but modeling them
42 in complex areas like the WL and GB is challenging. We present a new modeling strategy for
43 estimating fault slip rates in complex zones of active crustal deformation using data from GPS
44 networks. The technique does not rely on prior estimates of slip rates from geologic studies, and
45 only uses data on the surface trace location, dip, and rake. The iterative framework generates
46 large numbers of block models algorithmically from the fault database to obtain many estimates
47 of slip rates for each fault. This reduces bias from subjective choices about how discontinuous
48 faults connect and interact to accommodate strain. Each model iteration differs slightly in block
49 boundary configuration, but all models honor geodetic and fault data, regularization, and are
50 kinematically self-consistent. The approach provides several advantages over bespoke models,
51 including insensitivity to outlier data, realistic uncertainties, explicit mapping of off-fault
52 deformation, and slip rates that are more objective and independent of geologic slip rates.
53 Comparisons to the U.S. National Seismic Hazard Model indicate that ~80% of our geodetic slip
54 rates agree with their geologic slip rates to within uncertainties.

55

56 **Plain Language Summary**

57 The Walker Lane is a complex zone of faults in the western Great Basin of the western United
58 States that experiences frequent earthquakes driven by active plate tectonics. Ground networks

59 of very sensitive GPS stations deployed over the last few decades have collected data showing
60 where the ground deforms most quickly, and hence where earthquakes are more likely to occur.
61 Data on how fast faults slip over time is used to inform the public about the distribution and
62 intensity of the seismic hazard. In this study we present improved data and modeling that
63 resolve with unprecedented detail the rates, patterns, and styles of active crustal motion, resulting
64 in better estimates of fault slip rates in the Walker Lane. This work brings the picture of
65 earthquake potential derived from GPS networks into sharper focus, provides new information
66 about how plate tectonics works, and will lead to more accurate estimates of seismic hazard that
67 can help reduce the loss of life and property from earthquakes.

68

69 **1. Introduction**

70 In the Walker Lane and western Great Basin east of the Sierra Nevada Mountains active faults
71 accommodate ~20% of the Pacific/North America plate boundary relative motion (Dokka and
72 Travis, 1990; Thatcher et al., 1999; Bennett et al., 2003; Oldow, 2003). The fault system is
73 comprised of a complex set of active dextral, sinistral, and normal faults (Stewart, 1988;
74 Wesnousky, 2005; Faulds and Henry, 2008) that together work to release the accumulating
75 crustal strain (Figure 1). The faults are numerous, in places closely spaced and discontinuous,
76 and are linked to regional seismicity (dePolo, 2008; dePolo and dePolo, 2012). The system's
77 complexity creates a challenge for using measurements of active deformation from GPS geodesy
78 to estimate the slip rates on the faults.

79

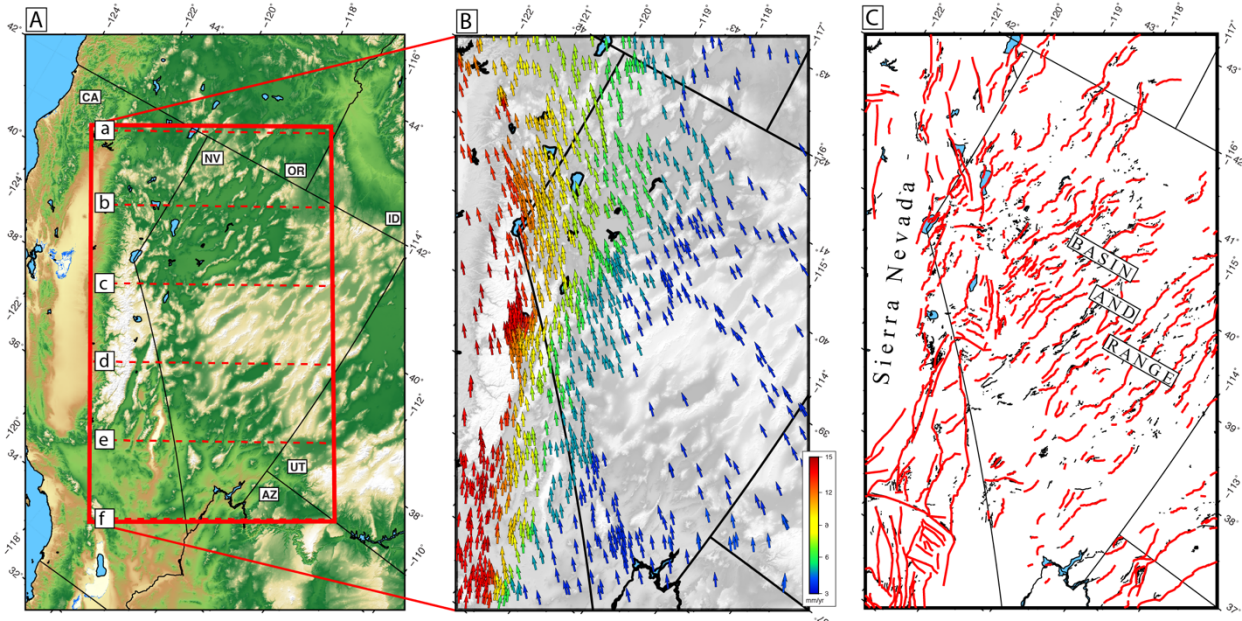
80 Fault slip rates are important for several reasons. For example, rates and azimuths of fault slip
81 are used to understand the kinematics of tectonics that drive processes within the plate boundary

82 zones (e.g., Weldon and Humphreys, 1986), and are used to compare to results of global plate
83 tectonic circuits (e.g., deMets and Merkouriev, 2016). Another reason that is of high societal
84 relevance is that slip rates are used in seismic hazard analysis, such as the US National Seismic
85 Hazard Maps (NSHM) project. In these hazard models the faults represent sources of elastic
86 moment that will be released in potentially damaging future ground shaking from earthquakes
87 (Frankel et al., 2002; Peterson et al., 2014; Field et al, 2023). For all these applications the
88 accuracy of the faults slip rates is essential.

89

90 However, the problem is challenging owing to gaps in the fundamental datasets, aleatory and
91 epistemic uncertainties in those data. Geodetic data can constrain the rate of interseismic strain
92 accumulation expected to be released in earthquakes but is limited by the short time of
93 observation (usually one to three decades). Nonetheless, they are a vital complement to other
94 data such as seismicity and earthquake geology which also constrain hazard (Shen et al., 2007;
95 Bird, 2009; Kreemer and Young, 2022). These data types each have their own strengths, sources
96 of uncertainty, community of practice, and offer reciprocal means for measuring active crustal
97 deformation. Comparisons between geologic, geodetic, and seismic moment rates reveal both
98 similarities between, and gaps among, the datasets (Ward, 1998; Pancha et al., 2006), suggesting
99 that approaches that take advantage of their individual strengths are needed.

100



101
102 **Figure 1.** A) Walker Lane and western Great Basin Region of the western United States, red box
103 indicates area covered in B) and C), red horizontal dashed lines a-f indicate location of profiles shown in
104 Figure 2. B) Median spatial filtered velocity field. Vectors are of constant length with color indicating
105 magnitude of velocity in a North America reference frame. C) Fault networks representing sources in the
106 USGS NSHM (Hatem et al., 2022a) (red) and other Quaternary faults (black). Supplemental Figure S1 is
107 a version of C annotated with fault names referred to in the text.

108
109 Integrated approaches have been attempted in a recent modeling exercise to support the latest
110 version of the US NSHM. A group of expert modelers developed solutions from the same input
111 database of western US fault geometries and GPS velocity field. They estimated slip rates for
112 faults in the database using their own various methodologies incorporating combinations of
113 geologic and geodetic data (Evans, 2022; Pollitz, 2022a; Shen and Bird, 2022; Zeng, 2022a).
114 Introduction and review of these models have been provided by Pollitz (2023b) and Johnson et
115 al., (2023). They point out that while the slip rate estimates exhibit broad similarity, they differ
116 in some important measures owing to multiple factors that sometimes result in high variability.
117 In those models the coefficient of variation for slip rates below 5 mm/yr (a category inside which
118 all WL faults lie) is above 2.0, indicating lack of agreement among the modelers at the level of
119 the uncertainties. Moreover, all the models incorporate geologic slip rates (Hatem et al., 2022b)

120 as additional constraints to regularize their inversions and so the resulting estimates are not
121 independent of geologic rates.

122

123 Here we address the slip rate problem by introducing a new block modeling method where block
124 geometries are repeatedly generated algorithmically from a given fault data base. In each
125 iteration the model starts with many blocks whose number are iteratively reduced to limit the
126 number of free parameters. These models are generated automatically in subdomains of the
127 region of interest, iterating with slightly different starting conditions so that large numbers of slip
128 rate estimates are made for each fault. While each individual model contains some of the usual
129 errors associated with model construction, the errors are different for each iteration and so are a
130 noise that is reduced by averaging over many models. However, the signals of fault slip rates are
131 similar in every model because they are present and have the same geometry in each iteration. In
132 this way the power of large numbers increases the robustness of the slip rate estimate to find the
133 set of kinematically consistent slip rate estimates that fit the data. The technique is like other
134 robust approaches that involve repeated sampling of the data to achieve estimates of velocity or
135 strain rates (e.g., Blewitt et al., 2016; Kreemer et al., 2018; Husson et al., 2018).

136

137 The degree of independence that the estimated geodetic rates have from geologic rates is an issue
138 with the NSHM deformation models identified in recommendations for future efforts (Johnson et
139 al., 2023). In our method described here geologic data from the NSHM (Hatem et al., 2022a) are
140 used to define the location, geometry, and style of fault segments, but not their slip rates. Thus,
141 agreements between our geodetic and geologic rates are corroborative, rather than the result of
142 an analytical constraint that they must be similar.

143

144 **2. Velocity Data**

145 We use horizontal position time series from the GPS holdings of the Nevada Geodetic
146 Laboratory (NGL, Blewitt et al., 2018) which are processed uniformly using the GipsyX
147 software (Bertiger et al., 2020). RINEX data are from networks listed in the Data Availability
148 Statement and include stations whose time series have duration longer than 2.5 years. We used
149 data products including daily reference frame alignment, orbit and clock files that were provided
150 by the Jet Propulsion Laboratory. More properties of the GPS data processing may be found in
151 Kreemer et al., (2020) and in the NGL GPS data analysis strategy and products summary
152 (<http://geodesy.unr.edu/gps/ngl.acn.txt>). We correct the time series for the effects of non-tidal
153 atmospheric, non-tidal ocean, and hydrological surface mass loading. These corrections have
154 been shown to reduce noise in GPS time series, especially in the vertical component, but also in
155 the horizontal component (Chanard et al., 2018; Martens et al., 2020). The corrections are based
156 on the predictions from the Earth System Modelling Group of GFZ Potsdam (Dill and Dobslaw,
157 2013), which are provided on a $0.5^\circ \times 0.5^\circ$ grid and interpolated onto the GPS station locations
158 and provided on the NGL GPS station pages. The trends of the time series represent motion with
159 respect to a fixed North American (NA) plate that has an Euler pole of rotation in the
160 International Terrestrial Reference Frame (Altamimi et al., 2016) defined by Kreemer et al.,
161 (2014). We obtain trends in station positions from the corrected time series with the MIDAS
162 robust non-parametric estimator, which is insensitive to steps, seasonality, outliers and
163 heteroskedasticity in the time series (Blewitt et al., 2016).

164

165 Additional campaign GPS data are taken from several sources that are listed in the Data
166 Acknowledgement section. While campaign GPS velocities tend to be less precise than those
167 from continuous stations, they have been shown in many studies to be precise enough to
168 constrain crustal movement. They are numerous and dense, enhancing geographic coverage of
169 the velocity field (e.g., Bennett et al., 1996; Thatcher et al., 1999; Oldow et al., 2003; Hammond
170 and Thatcher, 2005; McCaffrey et al., 2007; Spinler et al., 2010; Lifton et al., 2013; Murray and
171 Svanc, 2017, to name a few). We align these velocity solutions into the same North America
172 reference frame as the NGL MIDAS NA velocity field. Stations in clusters within $.001^\circ$ of one
173 another were combined into single rates by taking the median rate of the cluster. We include all
174 stations within 1° outside the model domain (Figure 1) to help constrain the reference frame
175 alignments between velocity fields and to reduce edge effects in the analysis that follows.
176 Together these networks provide 1311 stations inside the domain (421 continuous, 343
177 MAGNET semi-continuous, 547 campaign) (Figure 1). Like other recent analyses we impose a
178 velocity uncertainty floor of 0.1 mm/yr for both horizontal components to prevent very low
179 uncertainty velocities from having a disproportionately large influence on the inversions for slip
180 rates. Histograms of the east and north component velocities and their uncertainties are provided
181 in Figures S2 and in map view in Figure 1B and S3. A table of velocities and uncertainties is
182 provided in the Supplement (Table S1).

183

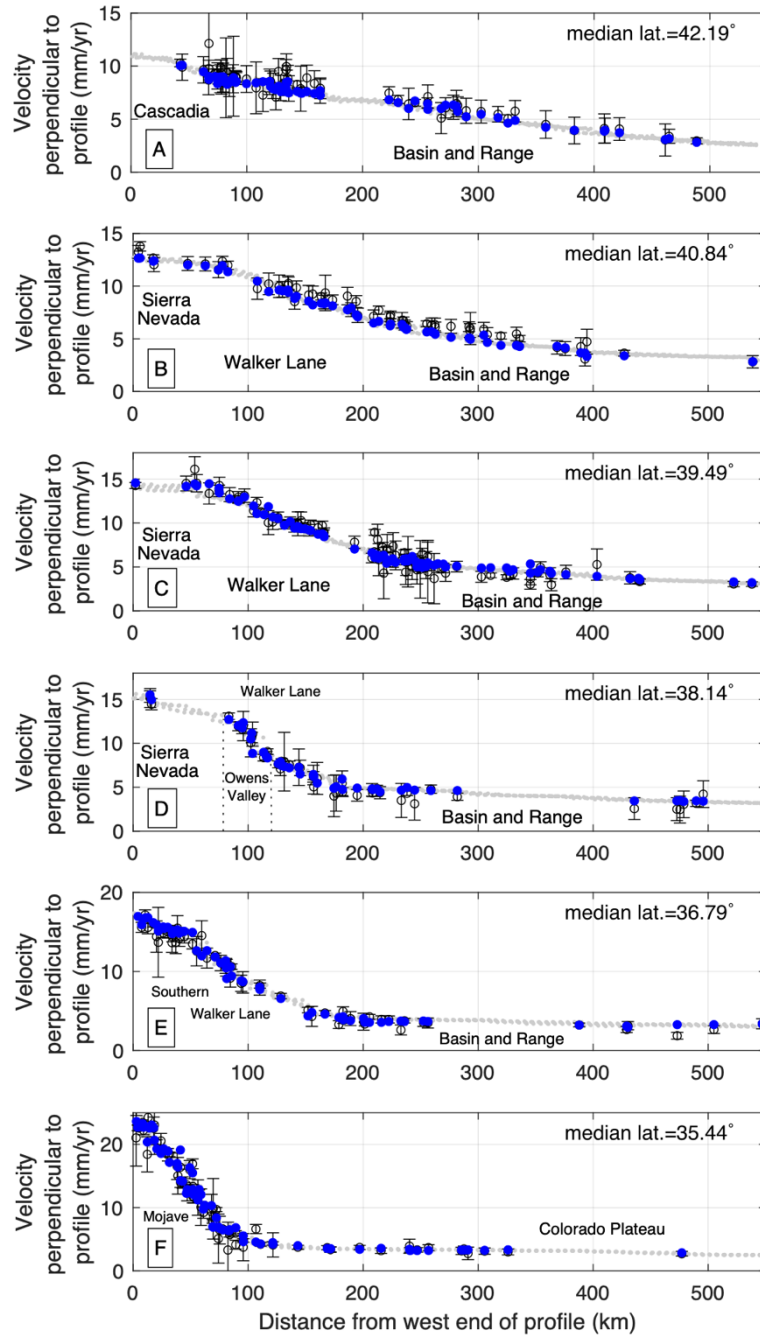
184 To omit outliers and noise from the velocity field we apply median spatial filtering to each
185 horizontal component. This process replaces each velocity with a weighted median of itself and
186 its neighbors, where the weight is a function of distance, data uncertainties, and a spatial
187 structure function (Hammond et al., 2016). The same process is used to image the velocities by

188 estimating at every point on a regular grid (spacing of $0.045^\circ \times 0.045^\circ$ or $\sim 5 \times 5$ km) the weighted
189 median of velocities from the nearest stations. The gridded field is used for the block modeling
190 because it is representative of the smoothly varying WL velocities and ensures that multiple
191 velocity estimates are present for even small blocks. The gridded field is shown in Figure S3.

192

193 Six profiles of velocity across the WL normal to the direction of Pacific and North America
194 relative plate motion show the patterns of the velocities and the magnitude of the signals with
195 respect to their uncertainties (Figure 2). The location of the 50 km wide profiles is shown in
196 Figure 1A. The gridded velocity is always within the uncertainty bounds of the station
197 observations, except in cases with obvious outliers. The profile-perpendicular velocities increase
198 to the west monotonically and their spatial gradient increases southward as the zone of
199 accommodation between the GB and WL narrows, consistent with previous studies (Kreemer et
200 al., 2012).

201



202

203 **Figure 2.** Velocity components perpendicular to the profile locations shown in Figure 1. Original
 204 velocities are shown with open circles and error bars with 2 times the uncertainties. Larger blue circles
 205 are the median spatial filtered velocities, the small gray dots are values from the gridded velocity field.
 206 Velocities parallel to the profile direction are provided in the Supplementary Figure S4. Some geographic
 207 features are annotated.
 208
 209

210 The component of velocity parallel to the profiles reveals smaller trends that change with
211 latitude, indicating changes in the azimuth motion of the Sierra Nevada/Great Valley microplate
212 (SNGV) from south to north (Figure S4). The change in sign of the trend is related to the
213 direction of motion and rotation of the SNGV, which results in away from the Pacific plate
214 motion in the south, and towards the Pacific plate motion in the north, consistent with the Sierra
215 Nevada microplate counterclockwise motion (Figure 1B) (e.g., Argus and Gordon, 1998; Dixon
216 et al., 2000; Bennet et al., 2003). This rotation sets the western boundary condition and exerts a
217 strong control on the strike and style of faulting east of the SNGV in the WL, which varies from
218 south to north.

219

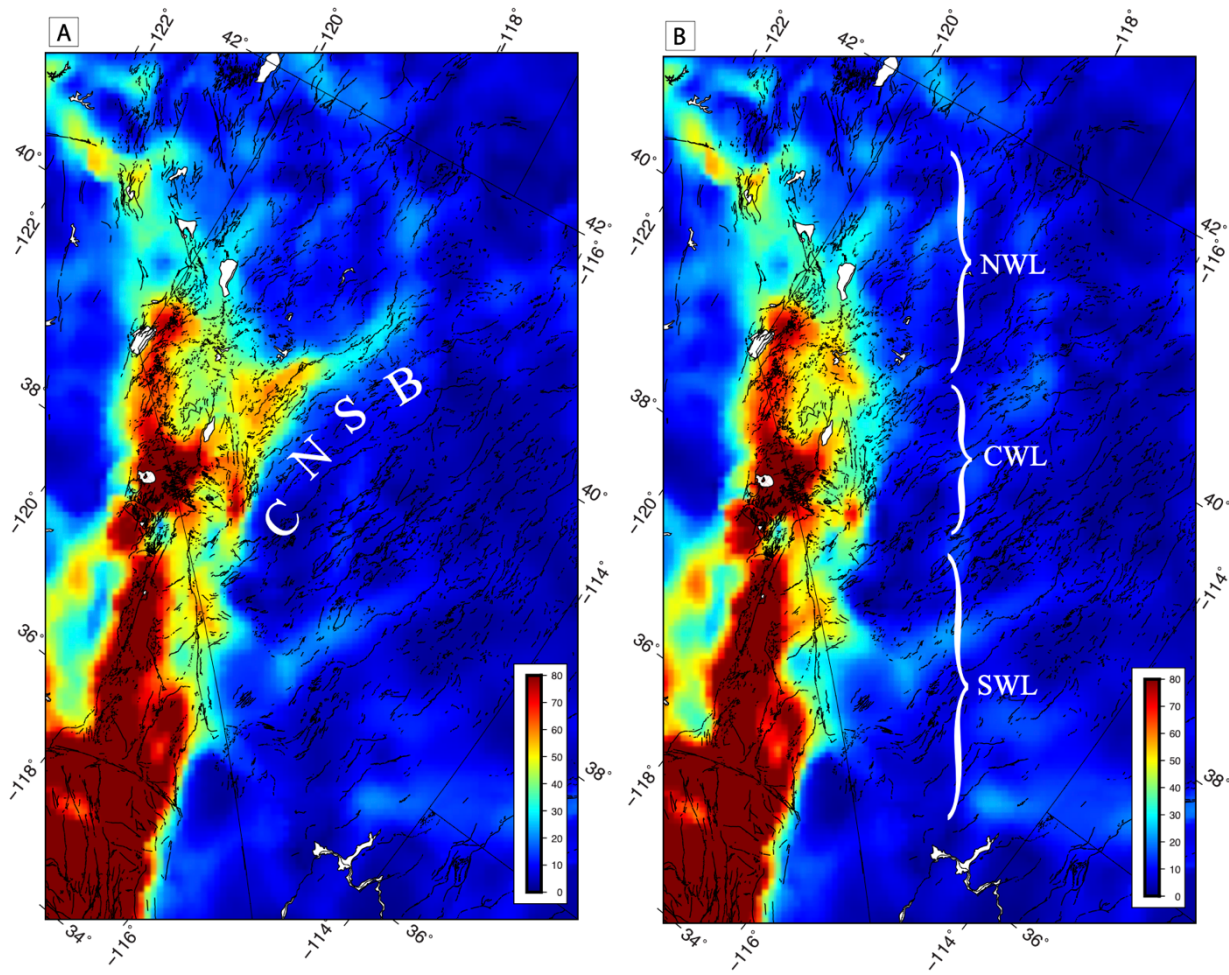
220 **3. Analysis**

221 **3.1 Strain Rates**

222 Maps of the tensor strain rate components of shear and dilatation depict the geographic variation
223 of strain accumulation which may eventually be released in earthquakes. In the fault slip rate
224 analysis described below, we use a strain rate map to provide a regularization to the block
225 modeling. Various kinds of parameterizations and regularizations for building strain rate maps
226 have been tested and compared (e.g., Beavan and Haines, 2001; Spakman and Nyst, 2002; Tape
227 et al., 2009; Hearn et al., 2010; Shen et al., 2015; Mauer and Materna, 2023). Our formulation
228 separates gradients in the GPS velocity field on a sphere into components of tensor deformation
229 and rotation using the parameterization of Savage et al. (2001). At each grid point we estimate
230 the local strain rate tensor with a linear inversion from the gridded horizontal velocities as input
231 data weighted with the velocity uncertainties. The results are insensitive to outlier velocity data
232 and irregularities in station spacing because the velocities have been spatially filtered and

233 gridded. Based on the result of an analysis of trade-off between high spatial resolution and low
 234 data misfit (Supplemental text and Figure S5) we adopted a length scale of 8 km for the shear
 235 and dilatational component stain rate maps (Figure 3). We depict the shear as the difference
 236 between principal strain rates ($\dot{e}_1 - \dot{e}_2$) and dilatation as the sum of principal strain rates ($\dot{e}_1 +$
 237 \dot{e}_2) (Figure 3).

238



239

240 **Figure 3AB.** A) Shear strain rates ($\dot{e}_1 - \dot{e}_2$), color scale is in nanostrains (10^{-9}) per year. White "C N S B"
 241 indicates strain anomaly associated with Central Nevada Seismic Belt earthquakes. B) Same map except
 242 with correction applied for viscoelastic postseismic relaxation from earthquakes of the. Black lines are
 243 Quaternary faults. Approximate extent of Southern (SWL), Central (CWL) and Northern Walker Lane
 244 (NWL) according to Faulds and Henry, (2008) are indicated with white curly braces. Fault names are
 245 given in Supplemental Figure S1.
 246

247 The contiguous band of high strain rates east of the SNGV is the geodetic signal of the WL, its
248 intensity decreases from south to the north. Its lower intensity in the Northern Walker Lane
249 (NWL) is a function of the wider and shallower gradient in GPS velocity compared to the
250 Southern Walker Lane (SWL) profiles (see B, C, D and E in Figures 1 and 2). The total velocity
251 difference across the system decreases from ~10 mm/yr in the SWL to ~7 mm/yr in the NWL.
252 Hence strain rates increase southward as a larger total velocity budget is accommodated across a
253 narrower zone.

254

255 We discuss other features of the WL strain rate maps in parts:

256

257 *In the Southern WL (SWL)* there are significantly higher strain rates in the Owens Valley ($>80 \times 10^{-9}/\text{yr}$) adjacent to the eastern SNGV than there are along other fault systems of the eastern WL
258 such as Death Valley, Furnace Creek, Fish Lake Valley, and Panamint Valley. This is
259 attributable to the higher gradient in GPS velocities adjacent to the SNGV (see profile D of
260 Figure 2). Strain rates across the Owens Valley are strongly transtensional, as seen in the
261 relatively high shear strain rate (Figure 3AB) and positive dilatation rates (Figure 3CD). This is
262 consistent with the strike of the Owens Valley (~N20°W) being in a releasing geometry with
263 respect to azimuth of SNGV motion (~N50°W) (as noted by Unruh et al., 2003). The higher
264 strain rates are more concentrated in the northern sections of the Owens Valley Fault and widen
265 to the south to distribute deformation more evenly across the southern Sierra Nevada, Little
266 Lake, Airport Lake, Panamint Valley, and southern section of the Death Valley Fault. The Death
267 Valley/Fish Lake Valley fault system has lower strain rates ($30-60 \times 10^{-9}/\text{yr}$) but are still elevated
268 above the rates in the GB east of the WL.

270

271 *In the Central WL (CWL)* the location and width of the zone of highest strain rates varies with
272 latitude. Just north of the SWL, the shear steps left and concentrates, passing through the Long
273 Valley Caldera near the SNGV (shown in detail in Hamond et al., 2019) and then widens again
274 northward. Here the higher shear strain rates occupy all the area between the SNGV and
275 northwest striking dextral fault systems east of Walker Lake such as Petrified Spring, Benton
276 Spring, and Gumdrop Hills faults (Wesnousky, 2005; Angster et al., 2020). However, shear rates
277 are highest at the east and west margins of the CWL, near the SNGV and east of the Wassuk
278 Fault. However, dilatation rates (Figure 3C) show faster extension near the western margin
279 adjacent to the SNGV and the Wassuk Fault. This is consistent with the partitioning between
280 shear and extensional domains (Surpless, 2008). However, it may be only a matter of degree
281 because the shear rates are lower west of the Wassuk but not zero, and the analyses of Bormann
282 et al., (2016) suggests that some strike slip through this part of the CWL is required to explain
283 the GPS data. At the left lateral faults in the Mina Deflection such as the Rattlesnake, Excelsior,
284 Candelaria Hills faults the shear strain rates are lower ($40 - 60 \times 10^{-9}/\text{yr}$) than those closer to the
285 SNGV, but are still higher than those in the GB to the east, where the strain rates drop
286 precipitously to below $10 \times 10^{-9}/\text{yr}$.

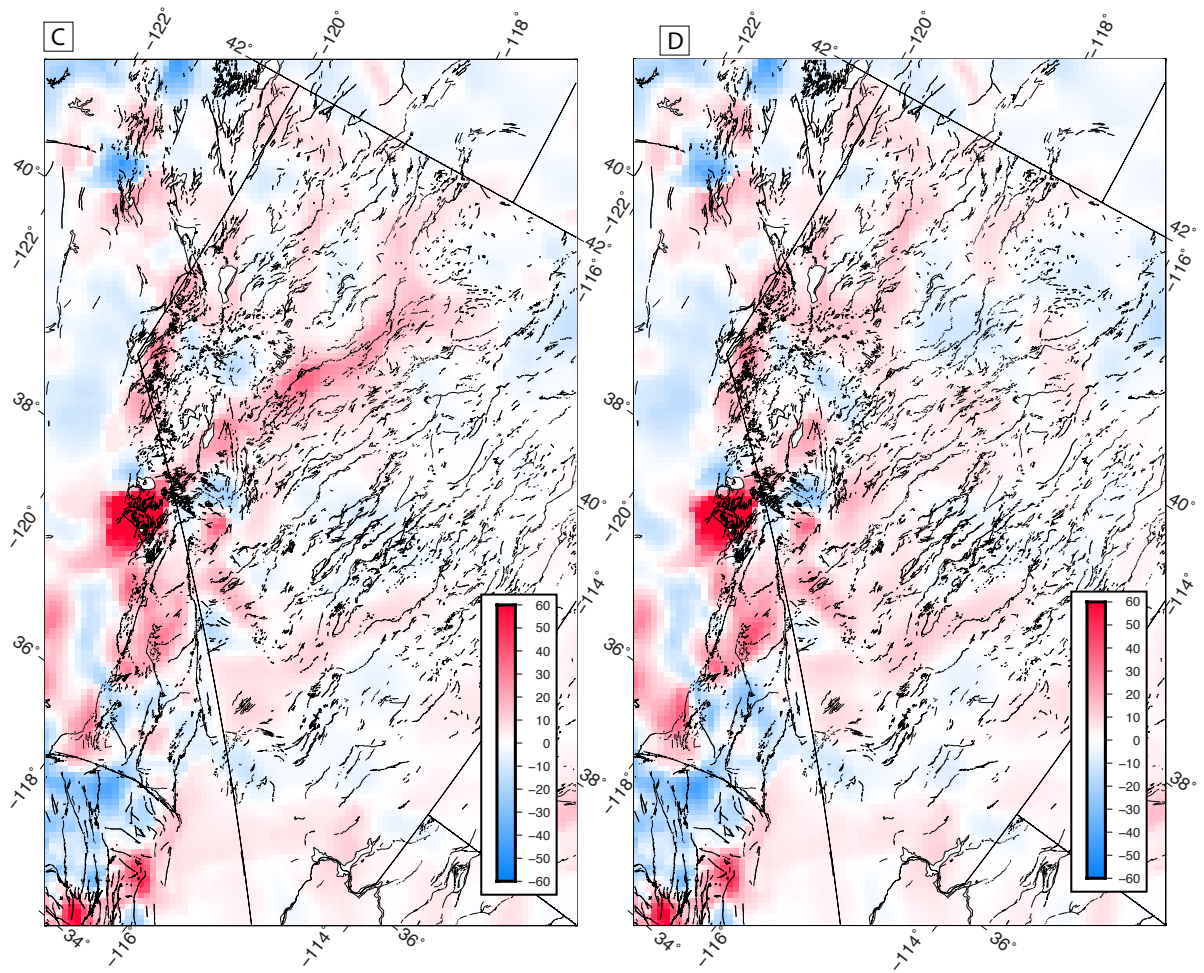
287

288 *In the Northern WL (NWL)* the strain rates separate and focus into two main arms, one in the
289 westernmost NWL overlapping the Lake Tahoe Basin adjacent to the SNGV, and the other
290 extending north-northeast to follow the Fairview, Dixie Valley and Pleasant Valley faults. This
291 zone is the location of a sequence of earthquakes that released most of the seismic moment in the
292 GB in the 20th century, known as the Central Nevada Seismic Belt (CNSB). In the next section

293 we discuss the transient nature of this active deformation feature. North of Lake Tahoe the NWL
294 shear strain rates are lower ($\sim 40 \times 10^{-9}/\text{yr}$) than to the south ($> 80 \times 10^{-9}/\text{yr}$) and confined to a
295 narrow zone between the Pyramid Lake and Mohawk Valley Faults, narrowing even further
296 north to lie between the Eagle Lake and Almanor Faults. Further north still a pocket of medium-
297 high strain rates ($\sim 50 \times 10^{-9}/\text{yr}$) lies at the Inks Creek, Battle Creek, and Bear Creek faults, a
298 place that may represent the locus of active convergence between the SNGV and crustal blocks
299 in the southern Cascadia forearc (Unruh et al. 2017; Angster et al., 2020).

300

301 *Along the east edge of the WL* eastward protrusions of elevated strain rates occur near locations
302 of east-northeast striking left-lateral faults such as in the Carson Domain near the Olinghouse
303 Fault, Mina Deflection, Gold Mountain east of the Death Valley Fault, and the Rock Valley Fault
304 south of Yucca Mountain. The Clayton Valley and Lone Mountain faults also have rates
305 slightly elevated compared to the rest of the GB east of the Death Valley fault, consistent with
306 the findings of Lifton et al., (2013) who detected extension normal to strike near the level of the
307 uncertainties with campaign GPS. The evolution of these faults may be linked to the nearby
308 strike slip systems of Fish Lake Valley/Death Valley (Oldow et al., 1994), suggesting that
309 perhaps all these protrusions are similar cases with similar mechanical origin. Significant strain
310 rates protruding east of the WL, elevated above background GB rates have been seen in other
311 recent strain rate models as well (e.g., Zeng, 2022b), and are especially apparent in maps made
312 with combinations of geodetic and geologic data (Kreemer and Young, 2022). These signals
313 may indicate that complexities exist in the deformation field in the GB east of the WL but are
314 currently near the resolution of the geodetic data, which may be clarified with better geodetic
315 coverage east of the WL and/or longer time series.



316

317 **Figure 3CD.** Same as Figure 3AB except for dilatational strain rate ($\dot{e}_1 + \dot{e}_2$), C) without correction for
318 postseismic deformation, D) with correction.

319

320

321 *Inside the SNGV* strain rates are very low (mostly $<10 \times 10^{-9}/\text{yr}$), consistent with previous
322 geodetic studies (Argus and Gordon, 1998; Dixon et al., 2000; Bennet et al., 2003; Kreemer et
323 al., 2012), lower levels of seismicity and sparsity of faults in the compilations (Figure 1C and
324 S1). The boundary between the low strain rates in the SNGV and the high strain rates in the WL
325 is very near the faults bounding the SNGV east edge. The most significant exception to the
326 SNGV rigidity is in the southernmost part of the microplate west of the SWL and Owens Valley,

327 where the Kern Canyon, Lake Isabella and western extension of the White Wolf faults extend
328 north of the Garlock fault into the High Sierra. Seismicity in this area has been used to suggest
329 that the southernmost Sierra is subject to heterogenous extension and crustal thinning associated
330 with foundering of lower lithosphere (Unruh et al., 2014).

331

332 The dilatational strain rate field indicates rates of area change that are generally lower than shear
333 strain rates (Figure 3CD) but are positive on average consistent with the WL and GB being a
334 transtensional part of the PA/NA plate boundary system. Owing to smaller signal to noise ratio
335 dilatation rate is harder to resolve than shear rate in the WL, but some clear patterns emerge.
336 Rates are faster in the WL than in the GB, and the stripe of faster extension adjacent to Sierra
337 coincides with zone of extension dominated transtension noted by Oldow (2003). Strong
338 positive dilatation is observed near the Long Valley Caldera active magmatic system that is
339 undergoes episodic inflation (Montgomery-Brown et al., 2015). This inflation affects a volume
340 of crust with active strain penetrating westward into the SNGV and eastward into the WL,
341 influencing seismicity which is transient deformation possibly not representative of long-term
342 deformation (Hammond et al., 2019).

343

344 **3.2 Correction for Viscoelastic Postseismic Relaxation**

345 Some signals in the geodetic data are not representative of the long-term rate and pattern of
346 deformation and must be removed from the velocity field before using if for an estimate of time-
347 invariant slip rates. An example in the WL and western GB is the post-earthquake relaxation
348 response to the late 19th and 20th century M 6.9-7.5 earthquakes in the Central Nevada Seismic
349 Belt (CNSB) (Wallace, 1984; Bell et al., 2004). It has been shown in several studies that these

350 events initiated an uplift and dilatation anomaly in central Nevada, which stand out from the
351 slow background rates in the rest of the Basin and Range (Gourmelen and Amelung, 2005). We
352 use a model of the viscoelastic relaxation process for the CNSB (Hammond et al, 2009) using the
353 theory and software of Pollitz (1997) to subtract the transient anomaly from the measured
354 velocities. The model accounts for the effects of nine earthquakes that occurred east of the
355 SNGV and within our area of study including the 1872 Owens Valley M7.4, 1915 Pleasant
356 Valley M7.3, 1954 Dixie Valley M6.9, 1954 Fairview Peak 7.0. The strain rate field corrected
357 for CNSB postseismic relaxation (Figure 3B and D) removes the long finger-shaped anomaly of
358 high shear and dilatational strain rate that branches north-northeast from the main band of high
359 strain rates northeast of the CWL. In the corrected strain rate maps, the eastern boundary of the
360 higher strain rates of the WL becomes much straighter and more parallel to its western boundary
361 (Figure 3B).

362

363 While the model removes the single most obvious north-northeast trending anomaly, we notice
364 the existence of several other lower intensity anomalies that extend in a similar direction to the
365 CNSB anomaly. One is near Pyramid Lake, NV and the other near Eagle Lake, CA, west of the
366 CNSB. Whether these reveal the unmodeled effects of earthquakes occurring possibly further in
367 the past is unknown. However, it is likely that not all events occurring in the last 1000 years on
368 WL faults are documented. Paleoseismic data show, however, that an event with ~3.3 m of slip
369 occurred on the Incline Village Fault in the northern Lake Tahoe Basin ~500±150 years before
370 present (Seitz et al., 2016). The amount of offset and length of the fault suggests a magnitude of
371 ~7.1. That would have been enough seismic moment to generate a postseismic viscoelastic
372 signal that is detectable with GPS, as in the CNSB. Whether that signal persists to the present day

373 and is related to the observed strain rate anomalies is speculative. There are other low amplitude
374 strain rate anomalies in both the shear and dilatation fields that are noticeable east of the WL,
375 where background strain rates are lower. However, some of these may be related to artifacts in
376 the imaging technique.

377

378 We do not attempt to correct the GPS velocity field for the magmatic inflation at LVC because
379 volcanic deformation is not a cyclic a deformation effect as is the case for faults. Inflation-
380 related deformation may be cumulative and influence nearby faults so should be modeled as part
381 of the strain accumulation field, and related slip rates.

382

383

384 **3.3 Block Modeling**

385 Block modeling assumes that the crust is divided into contiguous moving elastic volumes that
386 drive slip on the faults that bound them. The method accounts for the fact that the data are
387 collected during the interseismic period when fault systems are locked from the surface to the
388 bottom of the seismogenic upper crust but slip at the block motion rate at greater depth. The
389 parameterization enforces kinematic consistency between fault slip rates and crustal block
390 translation and rotation. Several implementations have been developed, varying in
391 parameterization, complexity, and use of regularization (e.g., Savage and Burford, 1973;
392 Matsu'ura et al., 1986; Bennett et al., 1996; McCaffrey, 2002; Meade and Hagar, 2005; Loveless
393 and Meade, 2010; Evans et al., 2015).

394

395 In the WL the block modeling approach is particularly challenging for a couple of reasons.

396 First, vertical-axis rotations of crustal blocks are observed in the Walker Lane and these rotations
397 are intimately linked to the fault slip. While paleomagnetic data constrain rotation since 10-13
398 Ma for some blocks (Cashman and Fontaine, 2000; Petronis et al., 2009; Carlson et al., 2013),
399 their present-day rates of rotation are not known, and data is not available for all WL areas.
400 Given the spacing between faults (5-30 km) and locking depths (~15 km) the signals of elastic
401 strain accumulation and rotation across the blocks spatially overlap. This leads to the solution for
402 block rotations and slip rates to be under-determined, with trade-offs between parameters.
403 Regulation of the problem is required, and our approach to this is explained below. Second, the
404 large number of faults and complexity of the fault system (Figure 1C) make building traditional
405 block models cumbersome. Block models generally require completely connected boundaries
406 that define independent polygonal domains. However, it is not always possible to define the
407 boundaries objectively because mapped fault traces are discontinuous, may be based on
408 incomplete datasets, and must be drawn according to subjective decisions from the analyst. We
409 address this difficulty in the next section.

410

411 **3.4 Model Generation, Iteration and Solution**

412 Here we generate block models algorithmically from a database of faults. We require that each
413 fault in the database be represented by an ordered sequence of coordinates that define the surface
414 trace, plus a dip and locking depth. We use the NSHM database of western US faults (Hatem et
415 al., 2022a) which provides these parameters. There are 373 faults in the database that touch the
416 study domain for which we estimate a slip rate (Figure 1). While not every known fault in the
417 GB is represented in this database, it includes the structures that are best studied and have been
418 demonstrated Quaternary active.

419

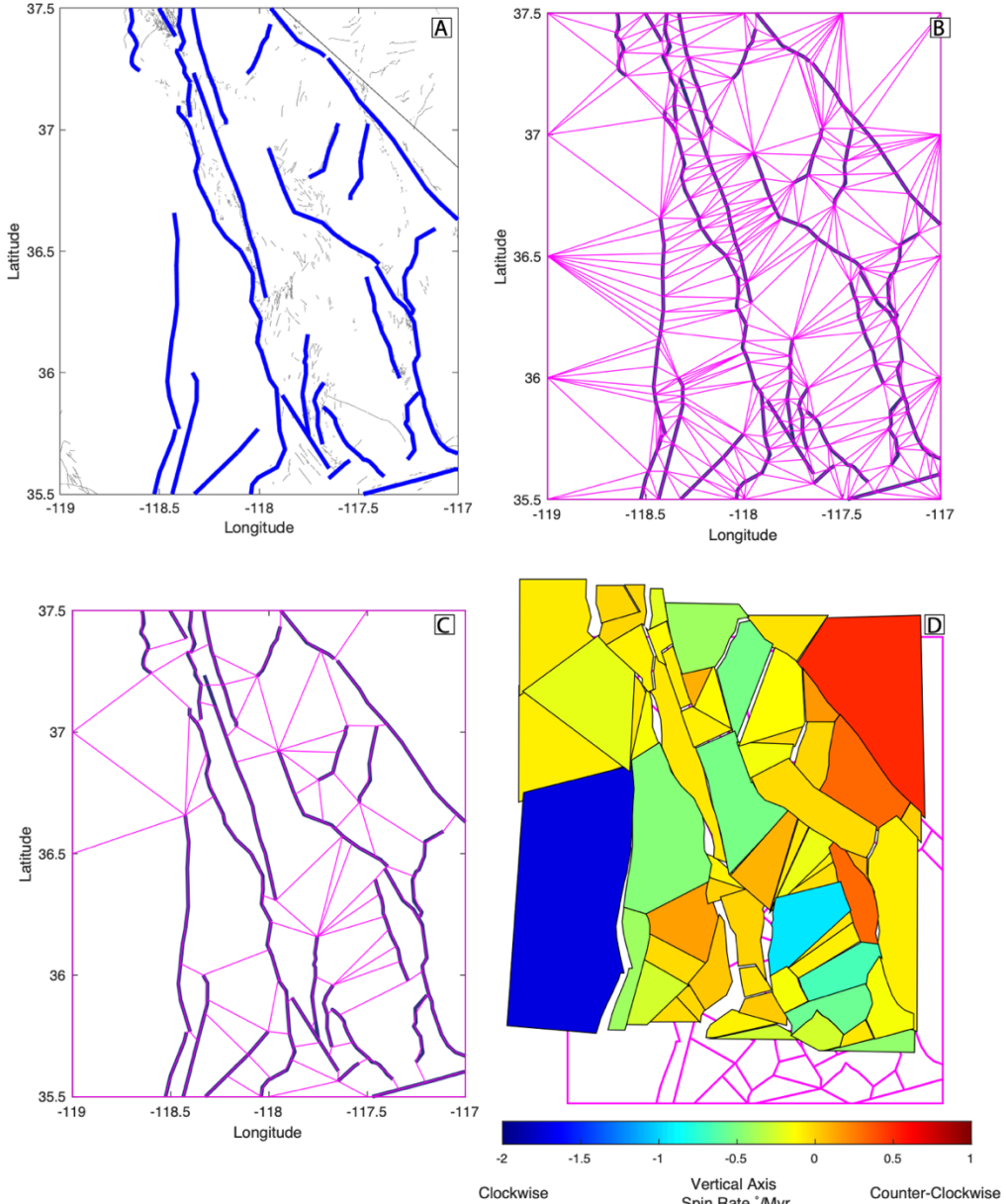
420 Prior to constructing each block model in our framework the fault traces are further simplified
421 beyond the already simplified traces available in the NSHM database (Hatem et al., 2022c). We
422 select a subdomain consisting of a latitude/longitude box of $2^\circ \times 2^\circ$ and truncate the fault traces
423 to include only those segments inside the box (Figure 4). We also down-sample the number of
424 nodes used to define fault traces so that each segment has length no smaller than ~one fortieth of
425 the dimension of the subdomain (0.05°). The spacing of segment nodes is controlled because
426 they define seed locations for the next step which is the generation of an initial set of blocks.

427 Nodes on the rectangular boundaries of each model are needed so that blocks can extend to the
428 edge of the domain. We place one at each corner and 3 more along each side so that the initial
429 configuration has blocks that are small enough to represent fault geometries. The result is a set
430 of nodes on the faults and boundaries that define a Delaunay triangulation where every fault
431 segment is the side of one of the triangles. Associating each fault segment with a triangle side
432 makes a valid block model that honors the fault network (Figure 4B). However, this model is
433 primitive because the presence of many small and narrow blocks makes it poorly parameterized
434 for deformation modeling. The model suffers from an excessive number of free parameters (3
435 Euler rotation vectors for each block) and the block rotations are difficult to constrain with GPS
436 velocity gradients because block dimensions may be small in one or more directions.

437

438 We reduce the number of blocks in the model by joining abutting blocks into single blocks and
439 repeating the process iteratively. At each iteration we prioritize which block pairs to combine by
440 developing a ranking system, where block bounding segments are scored according to their
441 geometric properties. Segments with low scores are selected for elimination, and the two

442 adjacent blocks are joined into one. Block boundary segments that align with faults are given
443 score of infinity so they cannot be lost through joining of blocks. Segments that are aligned with
444 the domain boundary are also given score of infinity. Segments that otherwise touch faults are
445 given a score equal to the number of fault segments touched, which preserves some detail in the
446 model near faults. Blocks are also targeted for combination if they have very small angles at
447 vertices (20° or less), small area (100 km^2 or less), large shape parameter defined as the
448 perimeter divided by the square root of the area (10 or more, where a circle is ~ 3.5), or large
449 interior angles (190° or more) which prevents blocks with significant concavity. Also blocks
450 having more than one contiguous chain of boundary nodes ('doughnut blocks') are forbidden by
451 not allowing any block merging that results in this condition. After a round of block number
452 reductions, the process is repeated until the number of blocks is small enough (less than 50
453 blocks), the number of blocks does not change, or the algorithm fails by generating a block
454 model that is invalid. The most common reason a block model is invalid is when it does not
455 correctly parameterize blocks with a sequence of nodes aligned with an adjacent block. This
456 condition can arise (rarely) owing to errors during the combination operation. Because of the
457 large number of models generated, loss of a few owing to block combination errors is acceptable.
458 An example of a block number reduction operation sequence is shown in Figure 4.
459
460



461

462 **Figure 4.** A) Faults of the southern Walker Lane in the NSHM database (blue), other Quaternary faults
 463 and CA/NV state line in gray. B) Initial Delaunay triangulation of nodes that represents primitive block
 464 model, C) blocks after reduction of number of blocks through iterative combination of neighboring
 465 blocks, D) solution for block motion from this model. Color indicates vertical axis spin rate component
 466 of the solution Euler pole for each block. Block movement is massively exaggerated to illustrate sense of
 467 relative motion, and strain accumulation at block boundaries is removed to emphasize rigid long-term
 468 component of motion.
 469

470 Our strategy for increasing robustness in the slip rate estimates is to generate many models to
 471 reduce dependence on any single model's representation of the fault network. While the

472 generation of each model is deterministic (the same fault inputs will always result in the same
473 block model geometries), small changes in the location of the bounding box with respect to the
474 faults result in a different initial node configuration and Delaunay triangulation. All models have
475 block boundaries that coincide with the input faults, but the other off-fault block boundaries
476 cross between the faults and boundaries in different places. We generate a grid of overlapping
477 rectangular model sub-domains with a spacing of $0.25^\circ \times 0.25^\circ$. At each iteration the subdomain
478 boundary is shifted by 0.25° which changes the relative position between the rectangular
479 boundary and the nodes along faults inside the boundary, resulting in a different triangulation.
480 The grid extends beyond the area of interest (Figure 1), but if the intersection between a sub-
481 domain and the full model domain (Figure 1) is <10% of the sub-domain area then the model is
482 not used. In all 1240 block models are built using the generative procedure described above and
483 1231 of them (99%) were valid and could be used to estimate slip rates from the GPS velocity
484 field.

485
486 For each block model we estimate a single slip rate on each fault segment using the method of
487 Hammond et al., (2011) that solves a regularized linear least squares inversion for a set of block
488 rotations and fault slip rates. In accordance with previous studies, we assume 15 km locking
489 depth throughout the entire area. No parameters for long term strain rates within individual
490 blocks are included. We apply a damping constraint regularization on slip rates and vertical axis
491 spin rates designed to stabilize the solutions. This is done by introducing another equation into
492 the system that damps each of the two components of slip rate (strike slip and dip slip) and the
493 vertical axis spin rate towards zero. For each fault the strength of this constraint is scaled by a
494 weight that is proportional to the local strain rate near the fault. For each block the spin rate is

495 also sensitive to the strain rate and accounts for the very large (orders of magnitude) differences
496 in strain rates in different parts of the model domain. These regularizations are detailed in the
497 Supplemental materials.

498

499 The median slip rates for each fault from the set of all block models in shown in Figure 5 and are
500 provided in Supplemental Table S2. Taking the median value reduces the impact of outliers that
501 can be seen in solutions of some individual block models (e.g., Figure 4B). Each fault has
502 multiple segments with some variability along strike so we consider each segment as an
503 individual sample of the slip rate which contributes to the distribution. Faults with a strike slip
504 component have a median number of 454 individual segments contributing to the slip rate
505 estimate (over all models and segments), but as few as 12 and as many as 3036. Long faults tend
506 to have more individual segments, and faults near the boundary have fewer since not as many
507 sub-domains cover them. There are fewer dip slip rates estimated because we did not estimate
508 them for faults which are deemed to be vertical strike slip faults in the NSHM database. Some
509 block models produce a slip rate that is inconsistent with the geologically determined sense of
510 slip for the fault. We truncate the distributions of slip rates in all cases where the slip rate has a
511 sign that is in direct conflict with the geological characterization of the fault rake and determine
512 the median rates from the remaining distribution.

513

514 **4. Results**

515 **4.1 Slip Rates**

516 For discussion we use the convention where dextral slip has negative and sinistral has positive
517 sign, normal slip has negative and thrust positive rates. For a given fault the slip rate we report is

518 the median slip rate for all segments and all block models that contribute an estimate. We
519 estimate the uncertainty with the median absolute deviation (MAD) of the slip rate estimate, and
520 then multiply by 1.4826 which makes the value like the standard deviation if the distribution of
521 slip rate estimates is Gaussian (Wilcox, 2005). This results in an uncertainty that account for
522 variability in fault strike and in the geometric depiction of the local block kinematics. We do not
523 divide by the square root of the number of model estimates as is done when estimating the
524 formal uncertainty in a mean because the large number of models generated (sometimes
525 thousands - Table S2) would make the uncertainties unrealistically small. Using the median and
526 MAD makes the rates and uncertainties less sensitive to outliers and representative of the body
527 of the data and model estimates. However, faults that have high degree of strike variability or
528 higher slip rates will tend to have larger uncertainties not because of greater error in the models,
529 but because the geometric variability along the fault maps to variability in slip rate, or their
530 geometries are difficult for the block generator to represent consistently. The resulting set of
531 fault slip rates reveals the distribution of active deformation into domains in the major sub-
532 provinces of the WL (Figure 5).

533

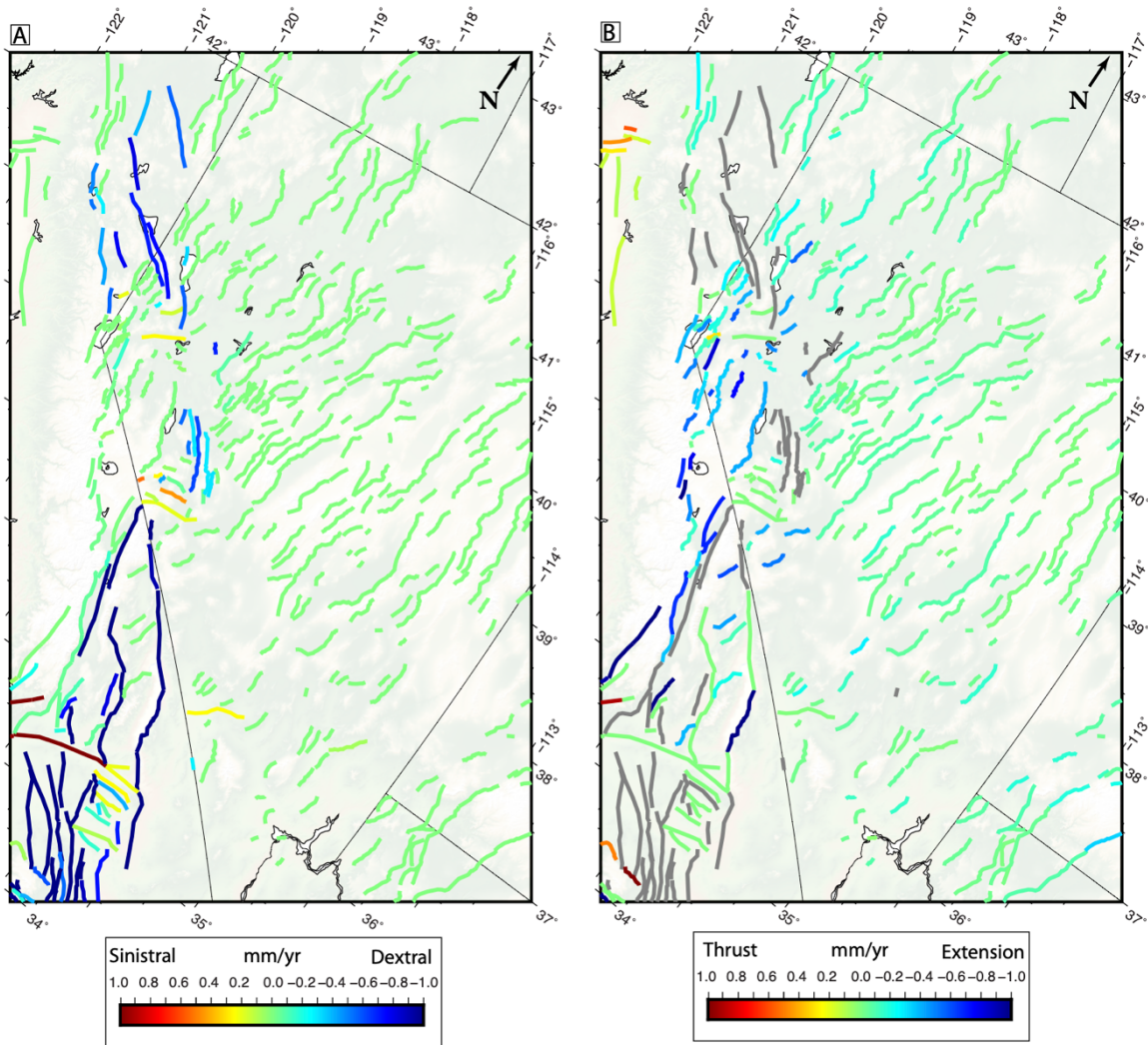
534 Strike slip rates are generally higher in the SWL, CWL and NWL compared to the rates in the
535 Basin and Range east of the WL. For example, in the SWL the long northwest striking dextral
536 faults accommodate the largest amount of deformation. The fastest dextral rate is -4.2 ± 1.4
537 mm/yr (dextral) for the Hunter Mountain/Saline Valley Fault, followed next by -2.9 ± 1.0 mm/yr
538 (dextral) for the Death Valley Black Mountains segment, -1.5 ± 0.6 mm/yr for the Owens Valley
539 Fault, and -0.8 ± 0.6 for the Panamint Valley fault. These faults account for most of the velocity
540 budget of across the SWL (Figure 2). While there is a strong contrast between high slip rates in

541 the SWL and low rates in the Basin and Range exclusive of the WL, some SWL slip rates are
542 low, even though they reside in areas with higher strain rates. For example, the extension rates
543 of the Deep Springs Valley (-0.4 ± 0.1 mm/yr), Dry Mountain (-0.2 ± 0.2 mm/yr), Tin Mountain ($-$
544 0.1 ± 0.1), Towne Pass (-0.6 ± 0.3) faults are systems that accommodate northwest-southeast
545 oriented extension amid the ranges that lie between the Death Valley, Panamint Valley, and
546 White Mountain fault systems.

547

548 In the CWL there is evidence of partitioning, where faster strike slip rates (faster than 1 mm/yr)
549 step right at the Mina Deflection from Fish Lake Valley and White Mountain into the Gumdrop,
550 Benton Springs and Bettles Well/Petrified Springs fault systems east of Walker Lake. This is
551 consistent with geological observations of fault rakes (Wesnousky, 2005; Surpless, 2008;
552 Angster et al., 2019; Pierce et al., 2021) and in our model is in part a consequence of the
553 imposing constraints on rake from the geologic database (Hatem et al., 2022a), which suppresses
554 strike slip on faults with rake = -90. The relatively high dextral slip rates stay to the east edge of
555 the WL until further north in the NWL, north of the latitude of Lake Tahoe, they become
556 distributed across the width of the WL between the SNGV and Pyramid Lake (Figure 5).

557



558

559 **Figure 5.** A) Strike slip component of fault slip rates in the WL, B) dip slip component (projected to
 560 horizontal). Gray colored faults are those for which the NSHM database prescribed it to be a vertical
 561 strike slip fault, so no dip slip component was estimated.
 562

563

564 In the NWL the higher dextral rates associated with the WL extend at least as far north as the
 565 northern end of the SNGV microplate, including the Lake Almanor, Eagle Lake and Likely fault
 566 systems. We see thrust sense on faults immediately north of the SNGV microplate, where it
 567 interacts with the Klamath Mountains and Oregon Coastal microplate at the Red Bluff, Bear
 568 Creek and Inks Creek faults, consistent with expectation based on other geodetic, geologic, and

569 seismic studies (Williams et al., 2006; Unruh and Humphrey, 2017; Angster et al., 2020). The
570 rate on the Hat Creek Fault to the north is slow and mostly normal sense (-0.1 ± 0.1 mm/yr).
571 Here, normal slip was not permitted on these faults since in the geologic database their dips were
572 90° .

573

574 The model images sinistral slip along the east-northeast striking faults that cross the WL and
575 reach to its eastern edge such as the faults of the Mina Deflection, Garlock and Olinghouse
576 faults, and Carson lineament. Sinistral slip on these structures is consistent with median model
577 clockwise vertical axis rotations that are discussed below, with expectation based on models of
578 blocks rotating in northwest directed shear field (McKenzie and Jackson, 1983; Platt and Becker,
579 2013; Bormann et al., 2016; deLano et al., 2019), and with observations of paleomagnetic
580 clockwise rotation (Cashman and Fontaine, 2000; Petronis et al., 2009; Carlson et al., 2013).
581 Sinistral slip is seen at the southern end of the SNGV at the White Wolf (4.2 ± 1.2) and Garlock
582 Faults (0.3 to 1.2 mm/yr increasing to the west). The Garlock fault slip rates are slower than
583 those estimated in most geologic studies, 2.7 to 5.3 mm/yr or higher, see Hatem and Dolan,
584 (2018) and references therein for a summary. We include only its central and easternmost
585 segments here, which are slower than its western section, in both this study and in geologic
586 observations (McGill et al., 2009).

587

588 Normal slip rates in the WL are also generally higher than normal slip rates in the Basin and
589 Range to the east, which are all closer to zero than -0.2 mm/yr. While the WL strain rate field is
590 dominated by shear, it also has enough positive dilatation and releasing bends in the fault
591 systems to drive normal slip. Some long faults have relatively fast normal slip rates with

592 uncertainties 0.5 mm/yr or less (e.g., northern Kern Canyon -1.4 ± 0.5 mm/yr). The very highest
593 normal slip rates are on shorter faults that tend to have high uncertainties (e.g., Hartley Springs at
594 -1.8 ± 1.5 and Airport Lake -1.3 ± 1.0 mm/yr). These are both in locations with multiple
595 intersecting or near-overlapping faults, so the block construction algorithm may be drawing
596 boundaries around these faults in a greater variety of ways. Extension occurs on most faults
597 north of the Garlock if they do not dip 90° in the fault database, on which normal slip was not
598 estimated (gray faults in Figure 5B). In the CWL normal slip is distributed between Lake Tahoe
599 and the Wassuk Fault near Walker Lake. In the area northwest of Lake Tahoe, between the
600 Mohawk Valley Fault and Pyramid Lake has positive dilatation, but the faults in the NSHM
601 database are all vertical strike slip faults, so normal slip was not estimated.

602 Normal slip on the Lone Mountain (0.6 ± 0.4 mm/yr), Clayton Valley (0.5 ± 0.4 mm/yr) and
603 Emigrant Peak (0.4 ± 0.3 mm/yr) faults, south of the Mina Deflection and east of the WL show
604 extension across the Silver Peak/Lone Mountain complex and appear consistent with
605 displacement-transfer style faulting (Oldow, 1992; Oldow 1994) and geological fault slip rates to
606 within uncertainty (Foy et al., 2012; Lifton et al., 2015).

607
608 In the Basin and Range east of the WL the median normal slip rate is -0.05 mm/yr and robust
609 measure of their standard deviation is 0.05 mm/yr. This suggests that the geodetically measured
610 deformation observed across the eastern Nevada Basin and Range (Hammond et al., 2014) is
611 discernable in the slip rates. It is also consistent with the strain release rate observed in
612 paleoseismic trenches on the active normal fault systems between 38.5° and 40.0° that
613 cumulatively add to between 0.8 to 1.0 mm/yr of extension across 450 km (Koehler and
614 Wesnousky, 2011). If ranges are separated by ~30 km then 450 km equates to 15 ranges or 0.07
615 mm/yr extension per range, similar to our median geodetic normal slip rate.

616

617 While Hammond et al., (2014) found a shear sense of strain rate in the geodetic data, there is no
618 systematic strike slip component in the slip rates estimated here or in the trenches of Koehler and
619 Wesnousky (2011). While the signal of extension is clear in the normal slip rates, there is a
620 possibility that our regularization based on scaling by our GPS strain rates model could be
621 suppressing the signal of strike slip since the strain rate in eastern Nevada is very low ($<5 \times 10^{-9}/\text{yr}$). Another possibility is that the shear observed in geodesy is a transient deformation
622 associated with the sum of many past and possibly distant western US earthquakes. This is
623 predicted by the forward model of Young et al., (2023) at a level below $2 \times 10^{-9}/\text{yr}$. Removing
624 their predicted postseismic strain from the observed strain rate makes it more uniaxial with an
625 east west extension direction similar to the geologic extension direction. Whether transients are
626 affecting the GB in this way deserves more direct study of the potentially far-reaching impact of
627 post-earthquake viscoelastic transients.

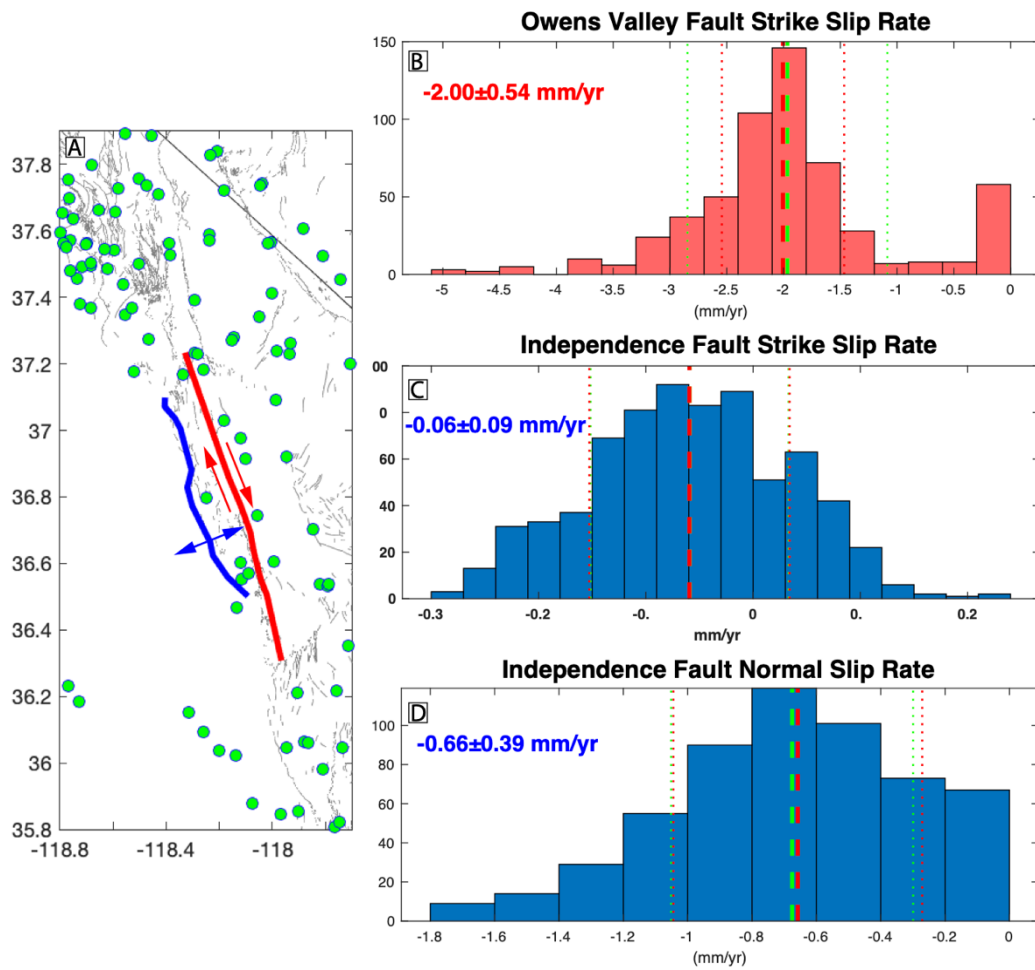
629

630 **4.2 Slip Partitioning**

631 We provide an example that shows the effectiveness of the method and regularization in
632 partitioning transtensional strain appropriately between closely adjacent strike slip and normal
633 faults. The Owens Valley fault is a vertical strike slip fault and is closely adjacent to (3-15 km)
634 the Independence Fault which is an east dipping normal fault that bounds the Sierra Nevada
635 range front (Figure 6). Their proximity means that the motion of the area between them must be
636 constrained in a robust way to accurately estimate both slip rates in a block model. Adding to
637 the challenge is the asymmetry in the strength of GPS data coverage, with strong network
638 coverage in the SWL to the east and weak coverage in the Sierra Nevada wilderness areas to the

639 west. Our method finds a strike slip rate for Owens Valley of -1.5 ± 0.6 mm/yr (dextral) and for
640 the Independence Fault -0.1 ± 0.1 mm/yr for its strike slip rate and -0.5 ± 0.30 mm/yr normal slip
641 rate. These rates are in accordance with geologic observations in terms of rates and style
642 (Beanland and Clark, 1994; Lee et al., 2001; Bacon and Pezzonpane, 2007; Jayko et al., 2009;
643 Haddon et al., 2016). While the normal component of slip on the Independence Fault is only
644 significant at the 1-sigma level, the higher level of uncertainty is to be expected here because of
645 the lack of GPS constraint west of the fault and the variability of its strike. This example
646 suggests that the combined power of the features of the method results in robust estimates of
647 fault slip rates that abide by geologic constraints, provide realistic uncertainties, without
648 explicitly constraining the rates to geologically determined rates a priori.

649



650

651 **Figure 6.** A) Owens Valley (red) and Independence (blue) Faults. Green circles are locations of nearby
 652 GPS stations, gray lines are Quaternary faults. B) Histogram of estimates of strike slip rate for Owens
 653 Valley Fault. No normal rate was estimated since it is categorized as a vertical strike slip fault in the
 654 geologic database. The green/red dashed vertical lines indicate the mean/median values in the
 655 distribution respectively. The Independence Fault strike slip rates are shown in C) normal component
 656 rates are shown in D). In B, C and D the green/red dotted vertical lines are ± 1 standard deviation from the
 657 mean and ± 1.4826 times the median absolute deviation from the median respectively.
 658

659 4.3 Vertical Axis Block Rotations

660 Rigid block motion on the surface of a sphere can be decomposed into two orthogonal
 661 components. The first is translation of the block associated with an Euler rotation vector 90°
 662 distant from the block centroid, the second is vertical axis spin which is associated with an Euler
 663 rotation vector parallel to the direction pointing to the block centroid from Earth center. For

664 each block we separate its estimated Euler rotation vector into these two components and then
665 using the vertical axis spin component estimate at each pixel on the map the median spin rate
666 from all the models (Figure 7).

667

668 The resulting image shows that in the WL spin is mostly clockwise with values less than $2^\circ/\text{My}$.
669 Pockets of faster spin rates occur near the locations of east-northeast sinistral faults, including
670 the Mina Deflection, Olinghouse Fault, Carson lineament, Garlock Fault and faults south of it.
671 The association between sinistral faulting and clockwise rotation is consistent with the
672 paleomagnetic data and models of rotations as noted in the previous section. There is also
673 clockwise rotation in the CWL west of the Wassuk Range Fault and east of Smith Valley of
674 $\sim 1^\circ/\text{My}$ consistent with other recent CWL block models (Bormann et al., 2016).

675

676 Even greater degrees of vertical axis spin rate are seen north of the SNGV. However, in this area
677 the geographic density of faults in the NSHM sources database is very low. For example, there is
678 an usually large gap between the Pondaosa proxy fault and the next fault to the west which is the
679 Trinidad Fault near the California coast 200 km west (off of map in Figure S1). Thus, clockwise
680 spin is needed to accommodate GPS velocity gradients that are part of the regional clockwise
681 rotation pattern between the SNGV and Oregon Coast microplate (Hammond and Thatcher,
682 2005; Williams et al, 2006; Unruh and Humphrey, 2017). Also, there is an unusually large gap of
683 74 km between the active Surprise/Warner Valley faults and Steens Mountain fault systems
684 (Personius et al., 2007; 2009) in which there is no fault in the sources database, though dozens of
685 shorter faults are present in the USGS QFFD (USGS and AGS, 2011; USGS and CGS, 2011;
686 USGS and NBMG, 2011; USGS and UGS, 2011). Here there are moderate clockwise rotation

687 rates in our model (-0.5 to -1.0°/Myr), possibly because of fewer faults are present in fault
688 database so the GPS velocity gradients tend to be accommodated through block rotation rather
689 than fault slip. If faults missing from the database are included in a future release, the rates of
690 block vertical axis spin needed to explain the GPS data may be reduced.

691

692 Crossing southern Nevada is a zone of positive (counter-clockwise) spin that follows a band of
693 seismicity that extends from southwest Utah to the SWL. Known as the Southern Nevada
694 transverse zone (Slemmons et al., 1965) it has been characterized with GPS measurements as a
695 zone of sinistral deformation transfer between the Wasatch Fault system and SWL called the
696 Pahranaghat Shear Zone (Kreemer et al., 2010). However, this band is in a zone where there is a
697 low density of fault segments in the database, and so high rotation may be imaged. Also, this
698 zone has lower GPS station density (Figure 1B), making it more difficult to resolve the zone's
699 location precisely. It does extend all the way to the Death Valley fault, and crosses it to the
700 Hunter Mountain/Saline Valleyly fault, encompassing Tin Mountain and Dry Mountain faults.

701

702

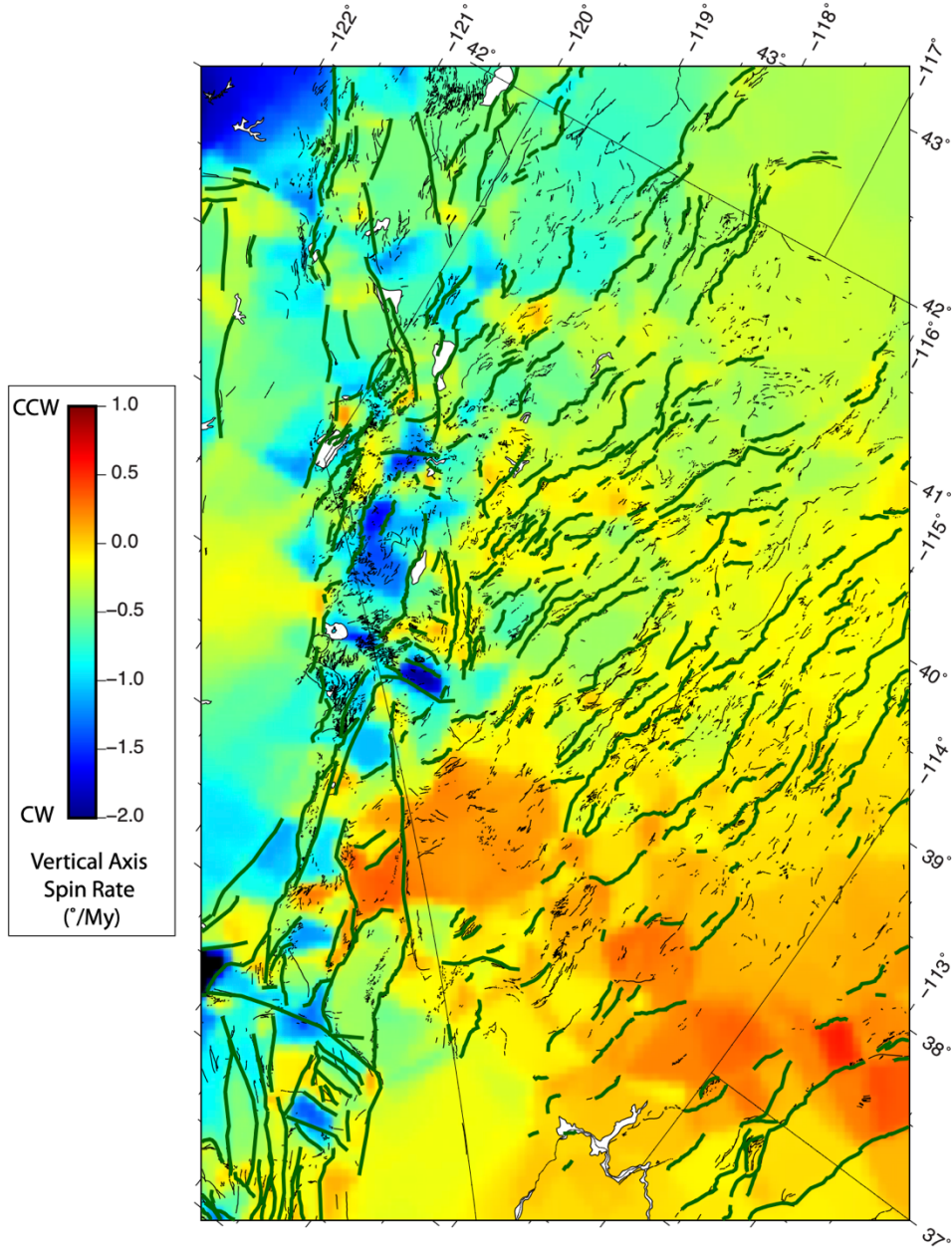
703

704

705

706

707



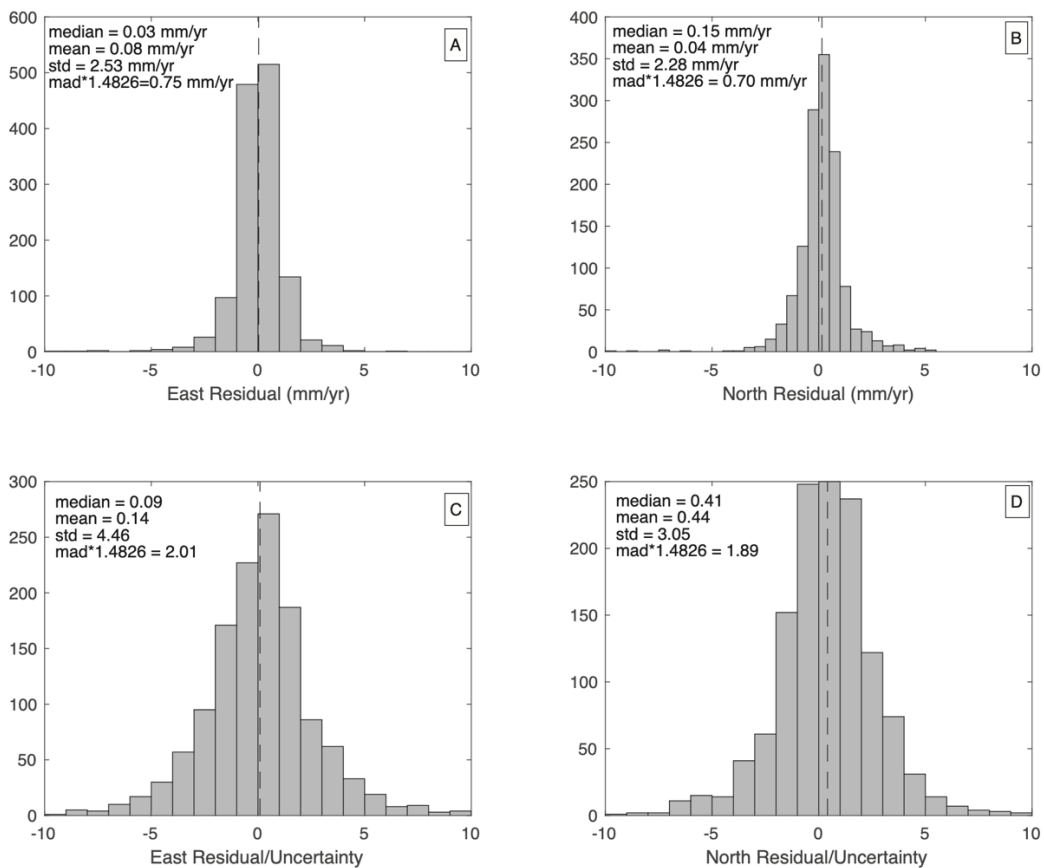
708

709 **Figure 7.** Image of median block vertical axis rotation rate. Color scale indicates rate and sign, positive
710 (red) is counter-clockwise, negative (blue) is clockwise.
711

712 **4.4 Model Uncertainties and Data Misfit**

713 Misfit of the models to the data is obtained by finding for each GPS station the median predicted
714 east and north velocity from the subset of block models that use the station. The residuals are the
715 difference between the original GPS velocities (not the gridded or filtered velocities) and the

716 predictions (Figure 8). The figure annotation shows the median absolute deviation (MAD) times
 717 1.4826 of residuals is significantly smaller than the standard deviation indicating that outliers
 718 affect the standard deviations substantially (by about a factor of 3 over the robust estimate made
 719 with the MAD). The histograms of residuals normalized by their uncertainties have
 720 MAD*1.4826 of ~2 indicating that the data are fit at a level about twice the uncertainties in the
 721 velocities, with a robust estimate of RMS of ~0.7 mm/yr. Our misfit is a bit lower than those in
 722 the NSHM western US models (Johnson et al., 2023) in part because we use the robust estimate
 723 which reduces impact of outliers and we focus on a subset of the western US with slower
 724 deformation.



725

726 **Figure 8.** Histograms of residual velocity in the east coordinate (left) and north coordinate (right). Top
 727 row indicates residuals in mm/yr, bottom row shows residual velocity components normalized by their
 728 individual component velocity uncertainties. See text for discussion.
 729

730 The histograms show near zero mean for the east and north residuals, with a slight tendency for
731 positive mean north residual at the level of ~0.1 mm/yr. To address the potential for systematic
732 misfit we use a definition of systematicity that for each station takes the mean dot product of
733 neighboring station velocities (defined by Johnson et al., 2023):

734

735
$$S_i = \left(\sum_{j=1}^n \frac{\vec{v}_i}{|\vec{v}_i|} \cdot \frac{\vec{v}_j}{|\vec{v}_j|} \right) / n \quad (1)$$

736

737 We use a radius of 30 km in the vicinity of each station i to select the n nearest stations. When
738 velocities have similar azimuths their dot products have higher magnitudes and S_i increases,
739 while when the vectors have random azimuths the signed dot product values tend to drive S_i
740 towards zero. This measure varies between 0 for very randomly oriented vectors to 1 when they
741 all have the same azimuth. The absolute value of S_i for each station is plotted in Figure 9A, and
742 reveals domains with significant systematicity, similar to the models that comprise the NSHM
743 deformation model suite (Johnson et al., 2023). However, this measure does not consider the
744 uncertainties in the velocities so may give the visual impression that large areas have systematic
745 residuals, even if the residual velocity magnitudes are below the uncertainties in the data.

746

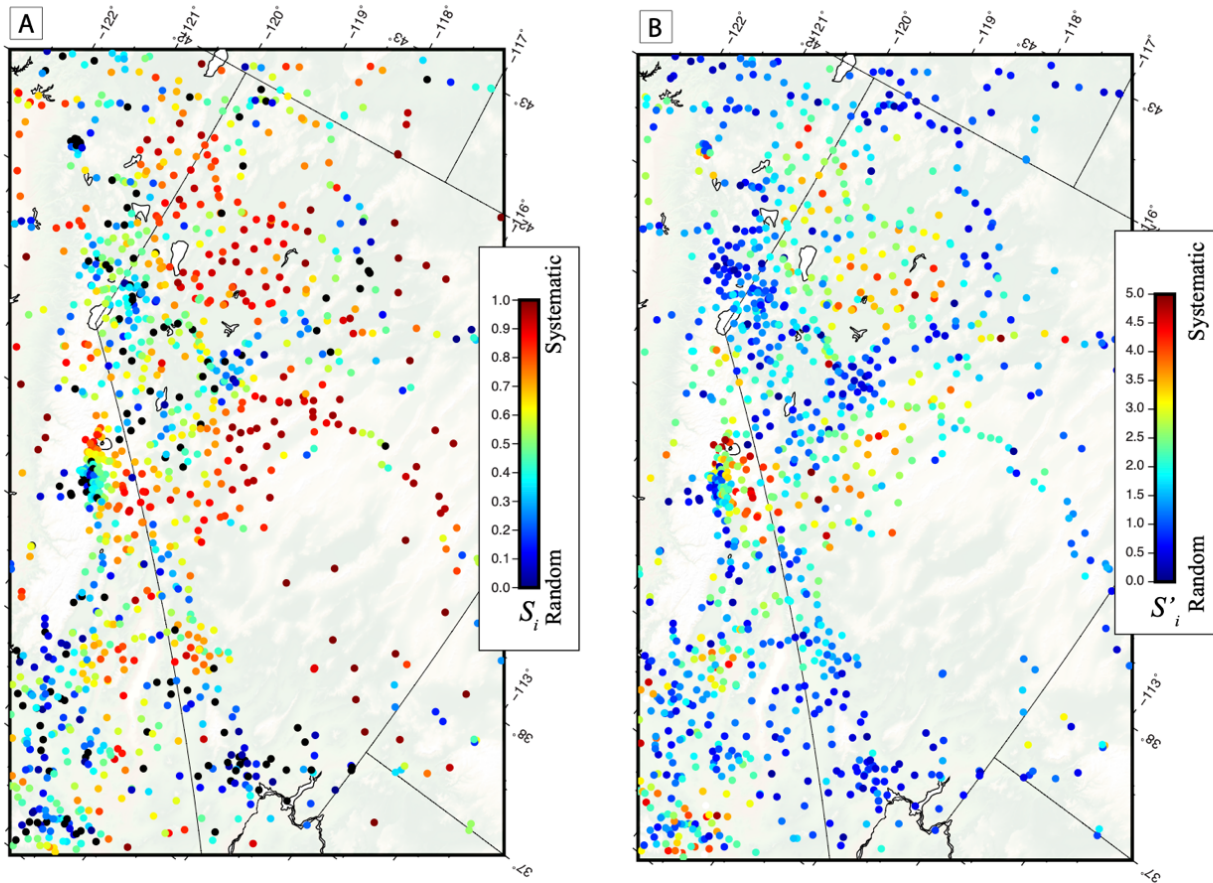
747 To address this we define an alternative version of the formula that normalizes the residual
748 vectors by their uncertainties instead of the residual norms:

749

750
$$S'_i = \left(\sum_{j=1}^n \sqrt{\frac{\vec{v}_i}{\sigma_{\vec{v}_i}} \cdot \frac{\vec{v}_j}{\sigma_{\vec{v}_j}}} \right) / n \quad (2)$$

751

752 When we look at Figure 9B which is based on equation (2) we see that many of the residuals that
753 were highly systematic in Figure 9A have residuals that are well below the uncertainties in the
754 velocity data. This is expected because these small residuals will not influence the least squares
755 inversions for block rotation and slip rate parameters as much as other more significant residuals.
756 There are, however, still a few significant systematic residuals in the vicinity of Long Valley
757 Caldera where magmatic inflation drives radial signals that are not well modeled on the CWL
758 fault systems. Also, in the NWL near the epicenters of the 1954 Fairview Peak and Dixie Valley
759 earthquakes, where the CNSB postseismic relaxation has been modeled and removed (see
760 Section 3.2), we see an indication of systematic misfit with $S' \sim 3\text{-}4$. This suggests that the signal
761 from CNSB postseismic relaxation may not be completely removed and some signal that is not
762 well modeled by CNSB faults remains. The third area with high S' values is east of the dextral
763 faults in the eastern CWL near the Toiyabe Range. This anomaly is near the source of the 1932
764 M7.1 Cedar Mountain earthquake, which is another events included in the CNSB transient
765 postseismic relaxation model and so may also be indicating that the transient signal is not
766 entirely removed.



767

768 **Figure 9.** A) Systematicity of residual values S_i . Color scale shows blue for randomly oriented residuals
 769 and red is for neighboring stations with very similar residual azimuth. B) is systematicity S'_i which
 770 normalizes the residual vectors by velocity uncertainty rather than residual vector magnitude. Both
 771 measures are unitless. When normalizing using velocity uncertainties the zones of systematic misfit are
 772 less extensive and occur areas with significant time-variable deformation.

773

774 **5. Discussion**

775 **5.1 Comparisons between geologic and geodetic slip rates**

776 Similarity between geologic and geodetic slip rates indicates that the different methods are
 777 estimating the same potential for slip at different times in the earthquake cycle, which increases
 778 confidence in the results. Because slip rates in the WL are slower than along the main plate
 779 boundary fault zones in western California, our slip rates occupy a much slower and narrower
 780 range than in other recent comparisons. It is therefore more challenging to establish a correlation

781 between geodetic and geologic rates in the WL. It is important to note that unlike in some other
782 studies (e.g., Pollitz, 2022; Zeng, 2022; Shen and Bird, 2022) we do not use geologic slip rates as
783 prior constraints or bounds on the solution for slip. Thus, our geodetic rates have a higher degree
784 of independence from the geologic rates and are corroborative of them when they agree.

785

786 We compare our geodetic slip rates to geologic rates from a recent compilation developed to
787 support the NSHM (Hatem et al., 2022b). We exclude faults south of 34.8° latitude and the
788 Garlock fault because its geologic rate in the NSHM database (up to 11 mm/yr) is much greater
789 than the range of all other faults in this study and our estimate (1.2 mm/yr in the central section).
790 The result (Figure 10A) shows a degree agreement but many slip rates are less than 1 mm/yr so
791 we also plot them on a \log_{10} axes (Figure 10B). The log scale plot reveals a general trend of
792 agreement between the geodetic and geologic slip rates. The correlation between slip rates is
793 similar on linear ($r=0.37$) and \log_{10} scales ($r=0.40$). This is a weaker correlation compared to
794 rates across the entire Western US, which are between 0.41 and 0.88 depending on the
795 contributing modeler (Johnson et al., 2023). However, a lower correlation is expected given the
796 far narrower range of slip rates in the WL (all are less than 5 mm/yr), and because we do not
797 impose a constraint in our modeling that our slip rates should be near the geologic rates.

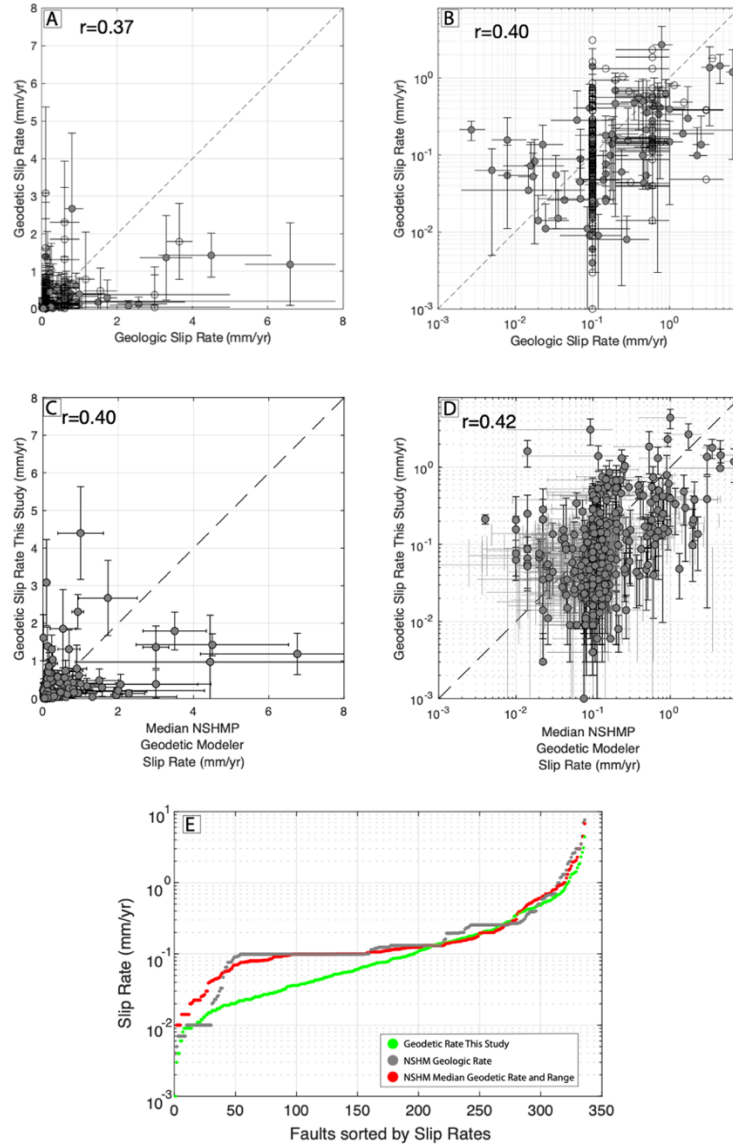
798 Nonetheless our conclusions are similar to what was observed for the entire western US: that the
799 faults with the lowest geologic rates (<0.05 mm/yr) have higher geodetic rates (Figure 10B). If
800 we reckon that slip rates agree when the geodetic rates are within the geologic
801 minimum/maximum bounds or when the geologic rates are within 2 times the geodetic
802 uncertainties, then 70 out of 362 slip rates (19.3%) disagree and the rest (80.7%) agree.

803

804 We also compare our geodetic rates to the median geodetic rates from the western US geodetic
805 modelers (Figure 10C and D). The correlations are slightly higher than the correlation with the
806 geologic rates, with $r=0.40$ for linear scale and $r=0.42$ for \log_{10} scale. Because we solve for the
807 same parameters from the same data, we may expect some agreement with their results.
808 However, many of the NSHM modelers optimized their analyses for 1) a much larger and more
809 tectonically diverse area with slip rates that vary by several orders of magnitude, 2) used a
810 variety of analytical techniques, and 3) used geologic rates as prior constraints. The similarity of
811 correlation shows that our rates agree with other geodetic slip rates about as well as they agree
812 with geological slip rates. This may possibly be because the NSHM modelers relied heavily on
813 geologic rates.

814
815 In the GB east of the WL, many of the faults have low slip rates, both in our model and in the
816 NSHM database. In this area many geologic rates in the NSHM database have slip rates exactly
817 0.1 mm/yr because they had no preferred rate, only a minimum of 0.0 mm/yr and maximum of
818 0.2 mm/yr. In these cases, we took the geologic rate to be the mean of the minimum and
819 maximum (Figure 10B). The geodetic rates for these faults vary between <0.01 mm/yr to over 1
820 mm/yr. The median difference between geologic and geodetic rates in this area is 0.03 mm/yr
821 which is close enough to zero to indicate that there is no bias for geologic or geodetic rates being
822 greater. The median absolute deviation of the differences is 0.10 mm/yr. The absolute level of
823 disagreement is very small mostly because there are so many faults in the Basin and Range with
824 very low slip rates, and any slip rate estimate consistent with the low background strain rate
825 would be similar at the level of 0.1 mm/yr. It is an advantage of our robust multi-block method

826 that it returns the geologically plausible slip rates for large areas of the GB with many low slip
 827 rates faults.



828

829 **Figure 10.** Comparison of geodetic slip rates from this study to A) slip rates from the geologic slip rate
 830 database (Hatem et al., 2022b) excluding the Garlock Fault, B) same as A) except with \log_{10} scale axes.
 831 The horizontal error bar gives the range of low to high geologic rate. If there is a preferred geologic rate
 832 it is plotted with a gray-filled circle, else an open circle is plotted at the mean between the low and high
 833 rates. Middle row shows comparison of geodetic slip rates from this study to C) geodetic slip rates from
 834 the NSHM geodetic deformation modelers as tabulated by Johnson et al., (2023). D) is same but on \log_{10}
 835 scaled axes. On all plots the vertical error bars are 2 times the uncertainty in our geodetic slip rates. E)
 836 shows the geodetic slip rates from this study (green circles), NSHM geodetic rates (red circles), and
 837 NSHM geologic rates (gray circles) sorted by slip rate. These curves show the similarity in distribution
 838 of the NSHM geologic and NSHM geodetic rates, and more continuous variation of slip rates from this
 839 study.

840

841 Lastly, in Figure 10E we compare the distributions of NSHM geologic and geodetic slip rates to
842 our geodetic rates. The faults in each set are sorted from smallest to largest slip rate value and
843 plotted in order. While it is difficult to show that our slip rates have greater accuracy compared
844 to the true slip rates, the distribution shows that they have a more natural diversity in slip rate
845 estimates especially below, and without clustering at, 0.1 mm/yr. The similarity in distribution
846 between the NSHM geodetic and geologic slip rates is likely a symptom of the dependence on
847 NSHM geologic rates.

848

849 **5.2 Off-Fault Deformation**

850 Wesnousky et al., (2012) showed that there are paths that can be walked from the Sierra Nevada
851 crest across the CWL that do not cross a mapped fault, suggesting that in some locations the
852 relative motion between the SNGV and GB is accommodated without faulting. Moreover, the
853 geodetic modelers for the western US NSHM explicitly quantified deformation in the GPS data
854 that was not mapped onto faults and derived off-fault moment rates between 31 and 58% across
855 the Western US. Off-fault deformation may represent strain in the deformation budget that
856 occurs near, but not on the main fault strands (Oskin et al., 2007; McGill et al., 2015), or
857 possibility entire crustal blocks undergo non-brittle deformation by developing folds or orocinal
858 flexures that accommodate strain (e.g., Faulds and Henry, 2008), or some other process.

859

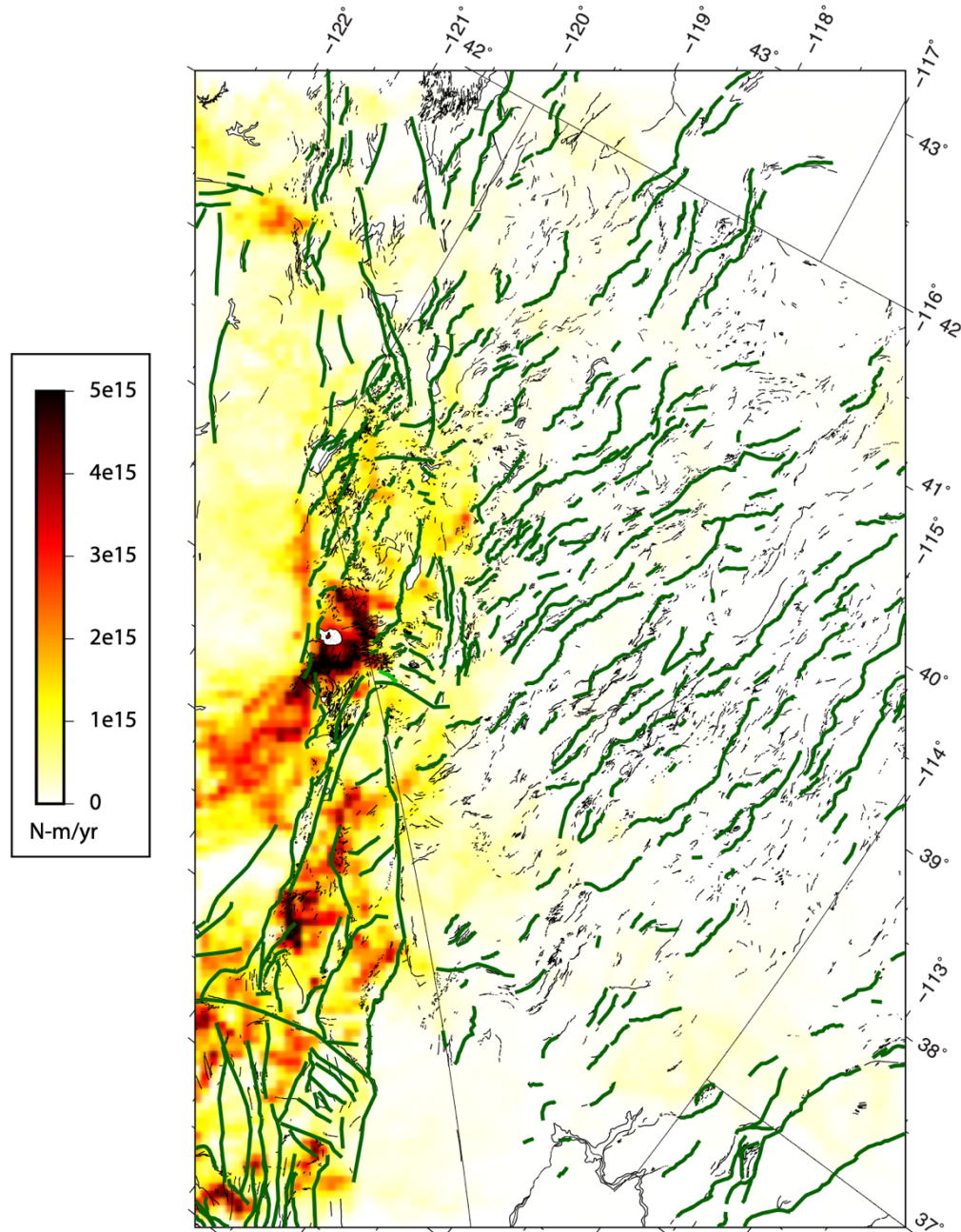
860 We estimate on-fault deformation as moment from slip on the active faults in the NSHM sources
861 database. We sum the moments by assuming a constant seismogenic thickness of $H=15$ km, a
862 shear modulus of $G=30$ GPa, and use fault areas of the locked segments $A = LW$, where $W =$
863 $H/\sin(\text{dip})$ and L is fault length. Summing over all faults segments the quantity $GHAs$, where s

864 is the slip rate gives a total on-fault moment of 4.3×10^{18} N-m in our model domain. We
865 estimate off-fault deformation by summing the same terms over all the boundaries between
866 blocks that are not in the NSHM database. The block boundaries are not guaranteed to occur in
867 the same place in every iteration or to have the same sign of slip. Thus, the off-fault moment is
868 distributed within zones between the NSHM model faults (Figure 11). The total off-fault
869 moment rate in the domain is 9.1×10^{18} N-m, giving an off-fault deformation proportion of 68%.

870

871 This proportion of off-fault deformation is higher than that found in western US models for the
872 NSHM (Pollitz, 2022a; Evans, 2022; Shen and Bird, 2022; Zeng, 2022a). There are two reasons
873 why the proportion may be particularly high in the WL. First, we include explicit
874 parameterization for off-fault deformation to occur, i.e., on block boundaries that are not faults,
875 and this allows the deformation to be detected and quantified. Second, in the WL and GB there
876 are likely more faults undiscovered and/or not included in the NSHM database, even though they
877 are active and contribute to the accommodation of far field budgets. Many faults in the USGS
878 QFFD (USGS and AGS, 2011; USGS and CGS, 2022; USGS and NBMG, 2011; USGS and
879 UGS, 2011) are not present in the NSHM database (Figure 11). Thus, the degree of
880 completeness of the fault database may be lower in the WL and GB compared to other systems
881 in the western US, e.g., the San Andreas. A recent example is the 2020 M6.5 Monte Cristo
882 Range earthquake in Nevada which ruptured the surface on unmapped segments of the
883 Candelaria Fault (Koehler et al., 2021).

884



885

886 **Figure 11.** Map of off-fault deformation rate. Dark green lines are faults from the NSHM database
 887 (Hatem et al., 2022a), other thin black lines are other faults in the USGS QFFD (USGS and AGS, 2011;
 888 USGS and CGS, 2022; USGS and NBMG, 2011; USGS and UGS, 2011).

889

890 The map of off-fault deformation (Figure 11) shows that there are higher levels in areas with
 891 high strain rates, e.g., in the SWL and ECSZ. Much of the imaged deformation is in zones that

892 are affected by time-variable processes such as the Long Valley Caldera and Coso magmatic
893 system (Wicks et al., 2001; Montgomery-Brown et al., 2015), and the southern Sierra Nevada,
894 which experiences hydrological loading (Hammond et al., 2016; Argus et al. 2017) and aquifer
895 related deformation (Hammond et al., 2016; Argus et al., 2017; Neely et al., 2019). Non-tectonic
896 processes contribute to the off-fault deformation field because they produce GPS velocity
897 gradients that cannot be well explained as slip deficit on fault systems.

898

899 We also see higher values where fault systems terminate and do not continue along another fault
900 system. For example, in the SWL there is a 36 km gap between the southwest end of the Deep
901 Springs Fault and the northern end of the Hunter Mountain/Saline Valley fault system. Here a
902 high amount of off-fault deformation is found in our model because the block models bridge
903 gaps with a boundary that accommodates relative motion between the NSHM faults. In east and
904 northwest Nevada some light-yellow patches indicate deformation inside wide gaps between
905 faults (Figure 11). Better characterizing off-fault deformation is a part of the recommendations
906 of Johnson et al, (2023), and recognizing where the slip rate models fail to explain deformation is
907 the beginning of better accounting for it in future models.

908

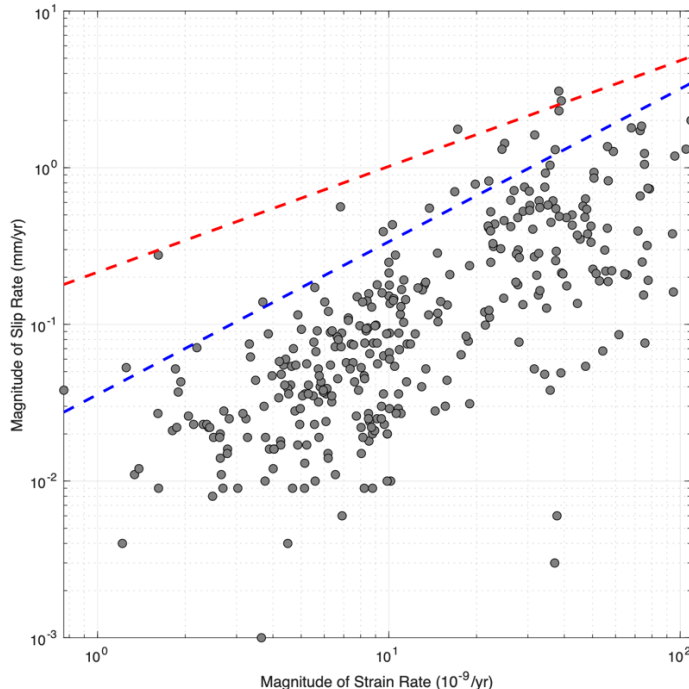
909 **5.3 Geodetic slip rates versus strain rate**

910 Slip rates tend to be higher in areas with higher strain rates. We can confirm that this is the case
911 in our model by plotting the magnitude of the slip rate as a function of the magnitude of the
912 strain rate near the fault. We define magnitude of strain rate as the norm of the tensor
913 components $\varepsilon_{mag} = \sqrt{\varepsilon_{xx}^2 + \varepsilon_{yy}^2 + 2\varepsilon_{xy}^2}$ (Kreemer et al., 2014). We exclude faults in Long
914 Valley Caldera because the high strain rates are from non-tectonic processes, and faults below

915 34.8° latitude because they include the San Andreas fault which has a very high slip rate. Strain
916 rates vary by orders of magnitude in the plate boundary, so we plot the values on a \log_{10} scale for
917 both axes in Figure 12. The correlation between magnitudes of strain rate and slip rate is
918 particularly strong in \log_{10} units, having $r=0.72$ (for linear scale $r = 0.50$).

919

920 If there is a strong correlation between strain rates and slip rates, this suggests that initial
921 estimates of fault slip rates can be made directly from the strain rate maps. This approach could
922 have utility in initializing deformation models that need prior values for slip rate inversions.
923 These initial values would be independent of geologic slip rates, preserving the independence of
924 the geodetic models. However, we observe that there are many cases where low slip rate faults
925 exist in high strain rate areas. In Figure 12 there are many faults where the strain rates are over
926 $50 \times 10^{-9}/\text{yr}$ but slip rates are below 1 mm/yr or even 0.1 mm/yr. These faults are near other
927 faults that are doing more to accommodate the deformation budget, possibly they are more
928 favorably located, oriented, or are more mature and mechanically efficient.



929

930 **Figure 12.** Scatterplot of slip rate magnitude versus strain rate magnitude using \log_{10} scale for both axes.
 931 Strain rates at Long Valley Caldera and all faults south of 34.7° are excluded. Red dashed line is slip rate
 932 envelope based on maximum of data, blue dashed line is similar but using the 95th percentile of the slip
 933 rates within strain rate bins. See equations (3) and (4) for formulas.
 934

935 Conversely, there are no faults in very low strain rate areas that have high slip rates (see the
 936 upper left corner of Figure 12). For example, when the strain rate is below $4 \times 10^{-9}/\text{yr}$ there are
 937 no faults with slip rates above 0.1 mm/yr, and when strain rates are below $10 \times 10^{-9}/\text{yr}$ there are
 938 no slip rates above 0.6 mm/yr. Thus, the relationship between strain rates and model slip rates
 939 suggests that there is an upper bound on slip rate that is a strong function of strain rate.
 940

941 If we consider the maximum value for slip rate magnitude (s_{mag}) inside 4 strain rate bins and use
 942 them to obtain an line fitting $\log_{10}(\epsilon_{mag})$ versus $\log_{10}(s_{mag})$ we get the red dashed line in Figure
 943 12. This line defines an envelope of the data above which there are almost no values for slip rate
 944 magnitude. The formula for the line is:
 945

$$946 \quad s_{mag,max} < 0.2072 \varepsilon_{mag}^{0.7334} \quad (3)$$

947

where strain rate magnitude ε_{mag} is in units of $10^{-9}/\text{yr}$ and slip rate magnitude s_{mag} is in mm/yr .

949 Equation (3) gives, for example, when $\varepsilon_{mag} = 10 \times 10^{-9}/\text{yr}$ a maximum slip rate bound of 1.12

950 mm/yr, and when $\varepsilon_{mag} = 100 \times 10^{-9}$ the maximum slip rate bound of 6.07 mm/yr.

951

952 The red line in Figure 12 describes an envelope based on maximum values of slip rates.

953 However, it is sensitive to outliers since it is based on least squares fit to the maximum slip rates

within bins. If we instead take the 95th percentile slip rate inside each of the 4 strain rate bins

955 we get the blue dashed line in Figure 12, whose formula is:

956

$$957 \qquad \qquad s_{mag,95} < 0.0347 \varepsilon_{mag}^{0.9922} \qquad (4)$$

958

959 This gives, for example, when $\varepsilon_{mag} = 10 \times 10^{-9}/\text{yr}$ then 95% of the slip rates will be below 0.34

960 mm/yr, and when $\varepsilon_{mag} = 100 \times 10^{-9}$ then 95% of the slip rates will be below 3.35 mm/yr. It

⁹⁶¹ may be prudent to use the 95th percentile version of the formula since its inference is less

962 sensitive to outlier slip rates. However, it will result in fewer high slip rates which could exist if

963 some faults slip faster than others with similar strain rates for e.g., mechanical reasons. Whether

964 there is a similar lower bound on slip rates is equivocal since the lower right area in Figure 12

965 has faults that slip between 0.001 to 0.1 mm/yr which are very slow and are the most difficult to

966 resolve geodetically.

967

968 There are caveats. For example, the slip rates in this study were derived using a regularization
969 that included applying a damping of slip rates that is a function of strain rate, and so could affect
970 the relationships in equations (3) and (4). However, the bulk of slip rates (~80%) agree with
971 geological slip rates, suggesting that they are appropriately regularized. The resolution of strain
972 rate maps varies with technique and are sensitive to assumptions about spatial smoothing
973 (Supplemental text and Figure S5) and could lead to differences in results when using these
974 formulas. The bounding envelopes are tuned to the WL where fault density is relatively high,
975 but the coefficients could be customized for other regions within plate boundary zones where
976 strain rates are higher, more variable or fault density is lower. However, the simplicity of these
977 relationships suggests that when strain rate maps are available, they may be conveniently used to
978 generate bounding a priori values for models of slip rates on faults in complex fault zones.
979 Alternatively, these relations could be used as a check on models, e.g., to identify model slip
980 rates that are unusually large outliers in a way that does not rely on geological slip rates.

981

982 **6. Conclusions**

983 We have presented a new method for estimating fault slip rates in areas of active tectonic
984 deformation that have many faults that comprise complex networks that may not completely
985 connect to describe contiguous blocks. The method uses an iterative algorithmically driven
986 construction of model block geometries to obtain many geodetic slip rates estimates for each
987 fault. The result obtains better sampling of the epistemic uncertainty associated with limited
988 knowledge of fault connectivity. The method includes constraining the models with a median
989 filtered and interpolated version of the GPS velocity field, applying regularization based on the
990 background strain rate estimated from GPS data.

991
992 We applied the method to the Walker Lane in the western Great Basin to obtain a robust set of
993 slip rates that agree with geologic slip rates in the USGS NSHM database to within uncertainties
994 ~80% of the time. This is achieved without constraining the slip rates to be the same as, or in the
995 range of the geologic rates. We also estimated the distribution of off-fault deformation which
996 tends to occur in areas with higher strain rates, areas where faults in the database do not connect
997 end to end to other faults, and in places where non-tectonic signals are present in the GPS
998 velocity data.

999
1000 Capacity for automatic block model generation and estimating slip rates in a robust way paves
1001 the way for larger scale application (e.g., entire Western US or world). Improving slip rate
1002 estimates based on geodesy alone will help objectify and strengthen seismic hazards estimates in
1003 complex fault systems.

1004
1005 **Data Availability Statement**
1006 RINEX data from the MAGNET GPS Network can be downloaded from
1007 <http://geodesy.unr.edu/magnet.php>. For the NSF EarthScope Network of the Americas data was
1008 downloaded from the UNAVCO archive (<https://www.unavco.org/data/gps-gnss/gps-gnss.html>).
1009 Additional GPS data was obtained from networks operated by the Arizona State Land
1010 Department, California Institute of Technology, Harvard-Smithsonian Center for Astrophysics,
1011 Hat Creek Radio Observatory, Institute of Geophysics and Planetary Physics at U.C.S.D., Jet
1012 Propulsion Laboratory at Caltech, Las Vegas Valley Water District, NOAA CORS Network and
1013 Earth System Research Laboratory, SmartNet North America, Trimble Navigation Limited, U.C.

1014 Berkeley, U.S. Coast Guard, U.S. Geological Survey, Utah Automated Geographic Reference
1015 Center, and Washoe County Public Works. We used the GipsyX software and data products
1016 including daily reference frame alignment, orbit and clock files provided by the Jet Propulsion
1017 Laboratory. Position time series and loading corrections for MAGNET and continuous GPS
1018 networks are freely available for download from <http://geodesy.unr.edu>. The predictions of non-
1019 tidal atmospheric, non-tidal ocean, and hydrological loading use products from the European
1020 ESMGFZ (<http://rz-vm115.gfz-potsdam.de:8080/repository>). We incorporated additional
1021 campaign velocity fields from GPS networks surveyed by the U.S. Geological Survey
1022 Earthquake Hazards Program, downloaded from <https://earthquake.usgs.gov/monitoring/gps>, and
1023 from tables in published studies (Williams et al, 2006; McCaffrey et al., 2013; 2016; Lifton et
1024 al., 2013; Spinler et al., 2010) including compilations (Shen et al., 2011; Kreemer et al, 2014;
1025 Sandwell et al., 2016). Fault data was obtained from Hatem et al., (2022a) downloaded from
1026 <https://doi.org/10.5066/P9AU713N> and from the USGS Quaternary Fault and Fold Database
1027 (USGS and AGS, 2011; USGS and CGS, 2011; USGS and NBMG, 2011; USGS and UGS,
1028 2011) downloaded from <https://www.usgs.gov/programs/earthquake-hazards/faults>.
1029

1030 Acknowledgements

1031 This work would not have been possible without steadfast support from the USGS Geodetic
1032 Networks program for data collection in the MAGNET GPS network under USGS NEHRP
1033 projects 08HQGR0027, G13AP0018, and cooperative agreements G10AC00138, G15AC00078
1034 and G20AC00046. Analysis was supported by USGS grant G17AP00004 and by NASA grants
1035 80NSSC19K1044 and 80NSSC22K0463. This work is in part based on services provided by the
1036 GAGE Facility, operated by EarthScope Consortium, with support from the National Science

1037 Foundation, the National Aeronautics and Space Administration, and the U.S. Geological Survey
1038 under NSF Cooperative Agreement EAR-1724794. Bret Pecoraro performed surveying at every
1039 station in the MAGNET GPS Network. Some figures were generated using the GMT software
1040 version 5 (Wessel et al., 2103). For Figure 1 we used color map GMT_seis cpt from cpt-city
1041 downloaded from <http://soliton.vm.bytemark.co.uk/pub/cpt-city/gmt/tn/>.

1042

1043 References

- 1044 Altamimi, Z., Rebischung, P., Métivier, L. and Collilieux, X. (2016). ITRF2014: A new release
1045 of the International Terrestrial Reference Frame modeling nonlinear station motions, *J.
1046 Geophys. Res. - Solid Earth*, 121, 6109–6131. <https://doi.org/10.1002/2016JB013098>.
- 1047 Angster, S., Wesnousky, S., Figueiredo, P., Owen, L. A., and Sawyer, T. (2020). Characterizing
1048 strain between rigid crustal blocks in the southern Cascadia forearc: Quaternary faults and
1049 folds of the northern Sacramento Valley, California, *Geology*, v. 49, p. 387–391.
1050 <https://doi.org/10.1130/G48114.1>.
- 1051 Angster, S.J, Wesnousky, S. G., Figueiredo, P. M., Owen, L. A., Hammer, S. J., (2019). Late
1052 Quaternary slip rates for faults of the central Walker Lane (Nevada, USA): Spatiotemporal
1053 strain release in a strike-slip fault system, *Geosphere*, 15 (5): 1460–1478.
1054 <https://doi.org/10.1130/GES02088.1>.
- 1055 Argus, D., and Gordon, R.G., (1998). Current Sierra Nevada-North America motion from very
1056 long baseline interferometry: Implications for the kinematics of the western United States,
1057 *Geology*, v. 19, p. 1085-1088.
- 1058 Argus, D. F., Landerer, F. W., Wiese, D. N., Martens, H. R., Fu, Y., Famiglietti, J. S., Thomas,
1059 B.F., Farr, T. G., Moore, A. W., Watkins, M. M. (2017). Sustained water loss in California's

- 1060 mountain ranges during severe drought from 2012 to 2015 inferred from GPS. *J. Geophys.*
1061 *Res.- Solid Earth*, 122, 10,559–10,585. <https://doi.org/10.1002/2017JB014424>.
- 1062 Bacon, S. N., and Pezzopane, S. K. (2007). A 25,000-year record of earthquakes on the Owens
1063 Valley fault near Lone Pine, California: Implications for recurrence intervals, slip rates, and
1064 segmentation models, *Geol. Soc. Am. Bull.*, 119(7–8), 823–847.
1065 <https://doi.org/10.1130/B25879.1>.
- 1066 Beanland, S., and Clark, M. M. (1994). The Owens Valley fault zone, eastern California, and
1067 surface rupture associated with the 1872 earth- quake, *U.S. Geol. Surv. Bull.*, 1982, 29 pp.
- 1068 Beavan, J. and Haines, J. (2001). Contemporary horizontal velocity and strain rate fields of the
1069 Pacific-Australian plate boundary zone through New Zealand, *J. Geophys. Res.*, 106(B1),
1070 741– 770. <https://doi.org/10.1029/2000JB900302>.
- 1071 Bell, J.W., Caskey, S. J., Ramelli, A. R. & Guerrieri, L. (2004). Pattern and rates of faulting in
1072 the Central Nevada Seismic Belt, and Paleoseismic Evidence for Prior Beltlike Behavior,
1073 *Bull. Seis. Soc. Am.*, v. 94, n. 4, pp. 1229–1254.
- 1074 Bennett, R.A., Rodi, W., Reilinger, R.E. (1996). Global Positioning System constraints on fault
1075 slip rates in southern California and northern Baja, Mexico, *J. Geophys. Res.* v. 101, B10,
1076 21,943-21,960.
- 1077 Bennett, R. A., Wernicke, B. P., Niemi, N. A., Friedrich, A. M., and Davis, J. L. (2003).
1078 Contemporary strain rates in the northern Basin and Range province from GPS data,
1079 *Tectonics*, 22(2), 1008. <https://doi.org/10.1029/2001TC001355>.
- 1080 Bertiger, W., Bar-Sever, Y., Dorsey, A., Haines, B., Harvey, N., Hemberger, D., Heflin, M., Lu,
1081 W., Miller, M., Moore, A. W., Murphy, D., Ries, P., Romans, L., Sibois, A., Sibthorpe, A.,
1082 Szilagyi, B., Vallisneri, M., Willis, P., (2020). GipsyX/RTGx, a new tool set for space

- 1083 geodetic operations and research, *Adv. Space Res.*, v. 66(3), p. 469-489,
1084 <https://doi.org/10.1016/j.asr.2020.04.015>.
- 1085 Blewitt, G., Kreemer, C., Hammond, W.C., Gazeaux, J. (2016). MIDAS Robust trend estimator
1086 for accurate GPS station velocities without step detection, *J. Geophys. Res.- Solid Earth*, 121,
1087 2054-2068. <https://doi.org/10.1002/2015JB012552>.
- 1088 Blewitt, G., Hammond, W.C. Kreemer, C. (2018). Harnessing the GPS Data Explosion for
1089 Interdisciplinary Science, *Eos*, 99. <https://doi.org/10.1029/2018EO104623>.
- 1090 Bormann, J., Hammond, W.C., Kreemer, C., Blewitt, G. (2016). Accommodation of missing
1091 shear strain in the Central Walker Lane, western North America: Constraints from dense GPS
1092 measurements, *Earth Planet. Sci. Lett.* 440, 169–177.
1093 <https://doi.org/10.1016/j.epsl.2016.01.015>.
- 1094 Carlson, C. W., Pluhar, C. J., Glen, J. M. G., & Farner, M. J. (2013). Kinematics of the west-
1095 central Walker Lane: Spatially and temporally variable rotations evident in the Late Miocene
1096 Stanislaus Group. *Geosphere*, 9(6), 1530–1551. <https://doi.org/10.1130/GES00955.1>.
- 1097 Cashman, P. H., & Fontaine, S. A. (2000). Strain partitioning in the northern Walker Lane,
1098 western Nevada and north-eastern California. *Tectonophysics*, 326, 11–130.
- 1099 Chanard, K., Fleitout, L., Calais, E., Rebischung, P., & Avouac, J.-P. (2018). Toward a global
1100 horizontal and vertical elastic load deformation model derived from GRACE and GNSS
1101 station position time series. *J. Geophys. Res. - Solid Earth*, 123, 3225–3237.
1102 <https://doi.org/10.1002/2017JB015245>.
- 1103 DeLano, K., Lee, J., Roper, R., and Calvert, A., (2019). Dextral, normal, and sinistral faulting
1104 across the eastern California shear zone–Mina deflection transition, California-Nevada, USA:
1105 *Geosphere*, v. 15(4), p. 1–34. <https://doi.org/10.1130/GES01636.1>.

- 1106 deMets, C. and Merkouriev, S., (2016). High-resolution reconstructions of Pacific–North
1107 America plate motion: 20 Ma to present, *Geophys. J. Int.*, 207, 741–773.
1108 <https://doi.org/10.1093/gji/ggw305>.
- 1109 dePolo, C. M. (2008). Quaternary Faults in Nevada, Nevada Bureau of Mines and Geology,
1110 University of Nevada, Reno, map 167, scale 1:1,000,000.
1111 <https://pubs.nbmng.unr.edu/Quaternary-faults-in-Nevada-p/m167.htm>
- 1112 dePolo, D.M, and dePolo, C. M., (2012). Earthquakes in Nevada, 1840s to 2010, Nevada
1113 Seismological Laboratory and the Nevada Bureau of Mines and Geology, University of
1114 Nevada, Reno, map 179, scale 1:1,000,000. <https://pubs.nbmng.unr.edu/Earthquakes-in-NV-1840s-to-2010-p/m179.htm>.
- 1116 Dixon, T.H., Miller, M., Farina, F., Wang, H., Johnson, D., (2000). Present-day motion of the
1117 Sierra Nevada block and some tectonic implications for the Basin and Range province, North
1118 American Cordillera, *Tectonics*, v. 19. n.1, 1-24, 1998TC001088.
- 1119 Dill, R., and Dobslaw, H. (2013). Numerical simulations of global-scale high-resolution
1120 hydrological crustal deformations, *J. Geophys. Res. - Solid Earth*, 118, 5008–5017.
1121 <https://doi.org/10.1002/jgrb.50353>.
- 1122 Dokka, R. K., Travis, C. J. (1990). Role of the Eastern California Shear Zone in accommodating
1123 Pacific–North America plate motion, *Geophys. Res. Lett.*, 17(9), p.1323-1326, 90GL01331.
- 1124 Evans, E., Loveless, J.P., Meade, B.J. (2015). Total variation regularization of geodetically and
1125 geologically constrained block models for the Western United States, *Geophys. J. Int.*, 202,
1126 713–727.

- 1127 Evans, E.L. (2022). A dense block model representing western continental United States
1128 deformation for the 2023 update to the National Seismic Hazard Model, *Seismol. Res. Lett.*,
1129 93(6), 3024–3036. <https://doi.org/10.1785/0220220141>.
- 1130 Faulds, J. E., & Henry, C. D. (2008). Tectonic influences on the spatial and temporal evolution
1131 of the Walker Lane: An incipient transform fault along the evolving Pacific–North American
1132 plate boundary, in Spencer, J.E., and Titley, S.R., eds. Ores and orogenesis: Circum-Pacific
1133 tectonics, geologic evolution, and ore deposits: *Arizona Geological Society Digest*, 22, 437–
1134 470.
- 1135 Field, E. H., Milner, K. R., Hatem, A. E., Powers, P. M., Pollitz, F. F., Llenos, A. L., Zeng, Y.,
1136 Johnson, K. M., Shaw, B. E., McPhillips, D., Thompson Jobe, J., Petersen, M. D., Shen, Z.-
1137 K., Evans, E. L. , Hearn, E. H., Shumway, A. M., Mueller, C. S., Frankel, A. D., DuRoss, C.,
1138 Briggs, R. W., Page, M. T., Michael, A. J. (2023). The USGS 2023 Conterminous U.S.
1139 Time-Independent Earthquake Rupture Forecast, in prep.
- 1140 Foy, T. A., Frankel, K. L., Lifton, Z. M., Johnson, C. W., and Caffee, M. W. (2012). Distributed
1141 extensional deformation in a zone of right-lateral shear: Implications for geodetic versus
1142 geologic rates of deformation in the eastern California shear zone-Walker Lane, *Tectonics*,
1143 31, TC4008. <https://doi.org/10.1029/2011TC002930>.
- 1144 Frankel A. D., Petersen, M. D., Mueller, C. S., Haller, K. M., Wheeler, R. L., Leyendecker, E.V.,
1145 Wesson, R. L., Harmsen, S. C., Cramer, C. H., Perkins, D. M., and Rukstales, K. S. (2002).
1146 Documentation for the 2002 update of the National Seismic Hazard Maps, Open-File Report
1147 02-420.
- 1148 Gourmelen, N., and Amelung, F. (2005). Postseismic mantle relaxation in the Central Nevada
1149 Seismic Belt, *Science*, 310, 1473-1476.

- 1150 Haddon, E. K., Amos, C. B., Zielke, O., Jayko, A.S. and Bürgmann, R. (2016). Surface slip
1151 during large Owens Valley earthquakes, *Geochem. Geophys. Geosyst.*, *17*, 2239–2269.
1152 <https://doi.org/10.1002/2015GC006033>.
- 1153 Hammond, W. C., and Thatcher, W. (2005). Northwest Basin and Range tectonic deformation
1154 observed with the Global Positioning System, 1999–2003, *J. Geophys. Res. - Solid Earth*,
1155 *110*, B10405. <https://doi.org/10.1029/2005JB003678>.
- 1156 Hammond, W. C., and Thatcher, W. (2007). Crustal deformation across the Sierra Nevada,
1157 northern Walker Lane, Basin and Range transition, western United States measured with
1158 GPS, 2000–2004, *J. Geophys. Res. - Solid Earth*, *112*, B05411.
1159 <https://doi.org/10.1029/2006JB004625>.
- 1160 Hammond, W.C., Kreemer, C., and Blewitt, G. (2009). Geodetic constraints on contemporary
1161 deformation in the northern Walker Lane: 3. Central Nevada Seismic Belt postseismic
1162 relaxation, *in* Oldow, J.S., and Cashman, P.H., eds., Late Cenozoic Structure and Evolution
1163 of the Great Basin – Sierra Nevada Transition, Geological Society of America, Special Paper
1164 447, p. 33–54. [https://doi.org/10.1130/2009.2447\(03\)](https://doi.org/10.1130/2009.2447(03)).
- 1165 Hammond, W. C., Blewitt, G., Kreemer, C. (2011). Block modeling of crustal deformation of the
1166 northern Walker Lane and Basin and Range from GPS velocities, *J. Geophys. Res.*, *116*,
1167 B04402. <https://doi.org/10.1029/2010JB007817>.
- 1168 Hammond, W.C., Blewitt, G., Kreemer, C. (2014). Steady contemporary deformation of the
1169 central Basin and Range Province, western United States, *J. Geophys. Res.*, *119*, 5235–5253,
1170 <https://doi.org/10.1002/2014JB011145>.

- 1171 Hammond, W.C., Blewitt, G., Kreemer, C. (2016). GPS Imaging of vertical land motion in
1172 California and Nevada: Implications for Sierra Nevada uplift, *J. Geophys. Res., - Solid Earth*,
1173 *121*, n. 10, p. 7681-7703. <https://doi.org/10.1002/2016JB013458>.
- 1174 Hammond, W.C., Kreemer, C., Zaliapin, I., Blewitt, G. (2019). Drought-triggered magmatic
1175 inflation, crustal strain and seismicity near the Long Valley Caldera, Central Walker Lane, *J.*
1176 *Geophys. Res. - Solid Earth*, *124*(6), p. 6072–6091. <https://doi.org/10.1029/2019JB017354>.
- 1177 Hatem, A. E., & Dolan, J. F. (2018). A model for the initiation, evolution, and controls on
1178 seismic behavior of the Garlock fault, California. *Geochem., Geophys., Geosys.*, *19*, 2166–
1179 2178. <https://doi.org/10.1029/2017GC007349>.
- 1180 Hatem, A.E., Collett, C.M., Briggs, R.W., Gold, R.D., Angster, S.J., Powers, P.M., Field, E.H.,
1181 Anderson, M., Ben-Horin, J.Y., Dawson, T., DeLong, S., DuRoss, C., Thompson Jobe, J.,
1182 Kleber, E., Knudsen, K.L., Koehler, R., Koning, D., Lifton, Z., Madin, I., Mauch, J., Morgan,
1183 M., Pearthree, P., Pollitz, F., Scharer, K., Sherrod, B., Stickney, M., Wittke, S., and
1184 Zachariasen, J., (2022a). Earthquake geology inputs for the U.S. National Seismic Hazard
1185 Model (NSHM) 2023 (western US) (ver. 2.0, February 2022): U.S. Geological Survey data
1186 release. <https://doi.org/10.5066/P9AU713N>.
- 1187 Hatem, A.E., Reitman, N.G., Briggs, R.W., Gold, R.D., Thompson Jobe, J.A., and Burgette, R.J.,
1188 (2022b). Western U.S. geologic deformation model for use in the U.S. National Seismic
1189 Hazard Model 2023, version 1.0: U.S. Geological Survey Data Release.
1190 <https://doi.org/10.5066/P9W63WOZ>.
- 1191 Hatem, A. E., Collett, C. M., Briggs, R. W., Gold, R. D., Field, E. H., Powers, P. M., and the
1192 Earthquake Geology Working Group (2022c). Simplifying complex fault data for systems-

- 1193 level analysis: Earthquake geology inputs for U.S. NSHM 2023, *Sci. Data* 9, 506.
- 1194 <https://doi.org/10.1038/s41597-022-01609-7>.
- 1195 Hearn, E., K. Johnson, D. Sandwell, and W. Thatcher (2010). SCEC UCERF Workshop Report,
- 1196 <http://www.scec.org/workshops/2010/gps-ucerf3/> FinalReport_GPS-UCERF3Workshop.pdf
- 1197 Hearn, E., (2022). “Ghost Transient” Corrections to the Southern California GPS velocity field
- 1198 from San Andreas Fault seismic cycle models, *Seis. Res. Lett.*, 93 (6): 2973–2989.
- 1199 <https://doi.org/10.1785/0220220156>.
- 1200 Husson, L., Bodin, T., Spada, G., Choblet, G., Kreemer, C. (2018). Bayesian surface
- 1201 reconstruction of geodetic uplift rates: Mapping the global fingerprint of Glacial Isostatic
- 1202 Adjustment, *J. Geodynamics*, 122, 25-40. <https://doi.org/10.1016/j.jog.2018.10.002>.
- 1203 Jayko, A.S., (2009). Deformation of the late Miocene to Pliocene Inyo Surface, eastern Sierra
- 1204 region, California, in Oldow, J.S., and Cashman, P., eds., Late Cenozoic structure and
- 1205 evolution of the Great Basin–Sierra Nevada transition: Geological Society of America
- 1206 Special Paper 447, p. 313–350.
- 1207 Johnson, K. M., Hammond, W. C. and Weldon, R. J. (2023). Review of geodetic and geologic
- 1208 deformation models for 2023 US National Seismic Hazard Model, accepted for publication
- 1209 in *Bull. Seis. Soc. Am.*
- 1210 Koehler, R.D., and Wesnousky, S. (2011). Late Pleistocene regional extension rate derived from
- 1211 earthquake geology of late Quaternary faults across the Great Basin, Nevada, between
- 1212 38.5°N and 40°N latitude, *GSA Bulletin*, v. 123, no. 3/4, p. 631–650.
- 1213 <https://doi.org/10.1130/B30111.1>.
- 1214 Koehler, R. D., Dee, S., Elliott, A., Hatem, A., Pickering, A., Pierce, I., and Seitz, G. (2021).
- 1215 Field response and surface-rupture characteristics of the 2020 M 6.5 Monte Cristo Range

- 1216 Earthquake, Central Walker Lane, Nevada, *Seismol. Res. Lett.* 92(2A), 823–839.
- 1217 <https://doi.org/10.1785/0220200371>.
- 1218 Kreemer, C., Blewitt, G., Hammond, W. C. (2010). Evidence for an active shear zone in
- 1219 southern Nevada linking the Wasatch fault to the Eastern California shear zone. *Geology*,
- 1220 38(5), 475–478. <https://doi.org/10.1130/G30477.1>.
- 1221 Kreemer, C., Hammond, W.C., Blewitt, G., Holland, A. Bennett, R.A., (2012). A geodetic strain
- 1222 rate model for the southwestern United States, scale 1:1,500,000, Nevada Bureau of Mines
- 1223 and Geology publication M178.
- 1224 Kreemer, C., Blewitt, G. and Klein, E. C. (2014). A geodetic plate motion and Global Strain Rate
- 1225 Model, *Geochem. Geophys. Geosyst.*, 15, 3849–3889.
- 1226 <https://doi.org/10.1002/2014GC005407>.
- 1227 Kreemer, C., Hammond, W. C., & Blewitt, G. (2018). A robust estimation of the 3-D intraplate
- 1228 deformation of the North American plate from GPS. *J. Geophys. Res.-Solid Earth*, 123,
- 1229 <https://doi.org/10.1029/2017JB015257>.
- 1230 Kreemer, C., Blewitt, G., Davis, P. M. (2020). Geodetic evidence for a buoyant mantle plume
- 1231 beneath the Eifel volcanic area, NW Europe, *Geophys. J. Int.*, 222, 1316–1332.
- 1232 <https://doi.org/10.1093/gji/ggaa227>.
- 1233 Kreemer, C., and Z. M. Young (2022). Crustal strain rates in the Western United States and their
- 1234 relationship with earthquake rates, *Seis. Res. Lett.*, 1–19.
- 1235 <https://doi.org/10.1785/0220220153>.
- 1236 Lee, J., Pencer, J., & Owens, L. (2001). Holocene slip rates along the Owens Valley fault,
- 1237 California: Implications for the recent evolution of the eastern California shear zone.
- 1238 *Geology*, 29, 819–822.

- 1239 Lifton, Z. M., Newman, A. V., Frankel, K. L., Johnson, C. W., and Dixon, T. H. (2013). Insights
1240 into distributed plate rates across the Walker Lane from GPS geodesy, *Geophys. Res. Lett.*,
1241 40, 4620–4624. <https://doi.org/10.1002/grl.50804>.
- 1242 Lifton, Z.M., Frankel, K.L., and Newman, A.V. (2015). Latest Pleistocene and Holocene slip
1243 rates on the Lone Mountain fault: Evidence for accelerating slip in the Silver Peak-Lone
1244 Mountain extensional complex: *Tectonics*, v. 34, no. 3, p. 449–463.
1245 <https://doi.org/10.1002/2013TC003512>.
- 1246 Loveless, J. P., and Meade, B. J. (2010). Geodetic imaging of plate motions, slip rates, and
1247 partitioning of deformation in Japan, *J. Geophys. Res.*, 115, B02410.
1248 <https://doi.org/10.1029/2008JB006248>.
- 1249 Martens, H.R., Argus, D.F., Norberg, C., Blewitt, G., Herring, T.A., Moore, A.W., Hammond,
1250 W.C., Kreemer, C. (2020). Atmospheric pressure loading in GPS positions: dependency on
1251 GPS processing methods and effect on assessment of seasonal deformation in the contiguous
1252 USA and Alaska, *J. Geodesy*, 94:115. <https://doi.org/10.1007/s00190-020-01445-w>.
- 1253 Matsu'ura, M., Jackson, D.D., Cheng, A. (1986). Dislocation model for aseismic crustal
1254 deformation at Hollister, California, *J. Geophys. Res.* v. 91, B12, p. 12,661-12,674.
- 1255 Maurer, J., and Materna, K., (2023). Quantification of geodetic strain rate uncertainties and
1256 implications for seismic hazard estimates, *Geophys. J. Int.*, v. 234, I. 3, P. 2128–
1257 2142. <https://doi.org/10.1093/gji/ggad191>.
- 1258 McCaffrey, R., (2002). Crustal block rotations and plate coupling, in *Plate Boundary Zones*, v.
1259 30, p. 101–122, eds S. Stein & J. Freymueller, AGU Geodynamics Series
- 1260 McCaffrey, R., Qamar, A. I., King, R.W., Wells, R., Khazaradze, G., Williams, C. A., Stevens,
1261 C. W., Vollick, J.J., Zwick, P.C. (2007). Fault locking, block rotation and crustal deformation

- 1262 in the Pacific Northwest, *Geophys. J. Int.*, 169, 1315–1340. <https://doi.org/10.1111/j.1365->
- 1263 246X.2007.03371.x.
- 1264 McCaffrey, R., King, R. W., Payne, S. J., and Lancaster, M. (2013). Active tectonics of
- 1265 northwestern U.S. inferred from GPS-derived surface velocities, *J. Geophys. Res. - Solid*
- 1266 *Earth*, 118. <https://doi.org/10.1029/2012JB009473>.
- 1267 McCaffrey, R., King, R. W., Wells, R. E., Lancaster, M., Miller, M.M. (2016). Contemporary
- 1268 deformation in the Yakima fold and thrust belt estimated with GPS, *Geophys. J. Int.*, 207, 1–
- 1269 11. <https://doi.org/10.1093/gji/ggw252>.
- 1270 McGill, S.F., Wells, S.G., Fortner, S.K., Kuzma, H. A., McGill, J. D. (2009). Slip rate of the
- 1271 western Garlock fault, at Clark Wash, near Lone Tree Canyon, Mojave Desert, California,
- 1272 *GSA Bulletin*, 121, 536-554. <https://doi.org/10.1130/B26123.1>.
- 1273 McGill, S. F., Spinler, J. C., McGill, J. D., Bennett, R. A., Floyd, M. A., Fryxell, J. E., and
- 1274 Funning, G. J., (2015), Kinematic modeling of fault slip rates using new geodetic velocities
- 1275 from a transect across the Pacific-North America plate boundary through the San Bernardino
- 1276 Mountains, California, *J. Geophys. Res. Solid Earth*, 120, 2772–2793.
- 1277 <https://doi.org/10.1002/2014JB011459>.
- 1278 McKenzie, D., and Jackson, J. (1983). The relationship between strain rates, crustal thickening,
- 1279 paleomagnetism, finite strain and fault movements within a deforming zone, *Earth Planet.*
- 1280 *Sci. Lett.*, 65, 182-202.
- 1281 Meade, B. J., and Hager, B. H. (2005). Block models of crustal motion in southern California
- 1282 constrained by GPS measurements, *J. Geophys. Res.* 110, B03403.
- 1283 <http://doi.org/10.1029/2004JB003209>.

- 1284 Montgomery-Brown, E. K., Wicks, C. W., Cervelli, P. F., Langbein, J. O., Svarc, J. L., Shelly,
1285 D. R., Hill, D. P., and Lisowski, M. (2015). Renewed inflation of Long Valley Caldera,
1286 California (2011 to 2014), *Geophys. Res. Lett.*, *42*, 5250–5257.
1287 <https://doi.org/10.1002/2015GL064338>.
- 1288 Murray, J. R., and Svarc, J. (2017). Global Positioning System data collection, processing, and
1289 analysis conducted by the U.S. Geological Survey Earthquake Hazards Program, *Seis. Res.*
1290 *Lett.*, *88* (3): 916–925. <https://doi.org/10.1785/0220160204>.
- 1291 Neely, W. R., Borsa, A. A., Burney, J. A., Levy, M. C., Silverii, F., & Sneed, M. (2021).
1292 Characterization of groundwater recharge and flow in California's San Joaquin Valley from
1293 InSAR-observed surface deformation. *Water Resources Res.*, *57*, e2020WR028451. <https://doi.org/10.1029/2020WR028451>.
- 1295 Oldow, J.S., (1992). Late Cenozoic displacement partitioning in the northwestern Great Basin, in
1296 Lane, C., and Steven, D., eds., Geological Society of Nevada Walker Lane Symposium:
1297 Structure, Tectonics and Mineralization of the Walker Lane: Reno, Nevada, Geological
1298 Society of Nevada, p. 17–52.
- 1299 Oldow, J.S., Kohler, G., Donelick, R.A., (1994). Late Cenozoic extensional transfer in the
1300 Walker Lane strike-slip belt, Nevada, *Geology*, v. 22, p. 637-640.
- 1301 Oldow, J. S. (2003). Active transtensional boundary zone between the western Great Basin and
1302 Sierra Nevada block, western US Cordillera. *Geology*, *31*(12), 1033–1036.
1303 <https://doi.org/10.1130/G19838.1>.
- 1304 Oskin, M., Perg, L., Blumentritt, D., Mukhopadhyay, S., and Iriondo, A. (2007). Slip rate of the
1305 Calico fault: Implications for geologic versus geodetic rate discrepancy in the Eastern

- 1306 California Shear Zone, *J. Geophys. Res.*, 112, B03402.
- 1307 <https://doi.org/10.1029/2006JB004451>.
- 1308 Pancha, A., Anderson, J.G., Kreemer, C., (2006). Comparison of seismic and geodetic scalar
1309 moment rates across the Basin and Range Province, *Bull. Seis. Soc. Am.*, v. 96, n.1, p. 11-32.
- 1310 <https://doi.org/10.1785/0120040166>.
- 1311 Personius, S. F., Crone, A. J., Machette, M. N., Mahan, S. A., Kyung, J.B., Cisneros, H., and
1312 Lidke, D. J., (2007). Late Quaternary Paleoseismology of the Southern Steens Fault Zone,
1313 Northern Nevada, *Bull. Seis. Soc. Am.*, v. 97, n. 5, pp. 1662–1678.
1314 <https://doi.org/10.1785/0120060202>.
- 1315 Personius, S. F., Crone, A. J., Machette, M. N., Mahan, S. A. and Lidke, D. J. (2009). Moderate
1316 rates of late Quaternary slip along the northwestern margin of the Basin and Range Province,
1317 Surprise Valley fault, northeastern California, *J. Geophys. Res.*, 114, B09405.
1318 <https://doi.org/10.1029/2008JB006164>.
- 1319 Petersen, M.D., Moschetti, M.P., Powers, P.M., Mueller, C.S., Haller, K.M., Frankel, A.D.,
1320 Zeng, Yuehua, Rezaeian, Sanaz, Harmsen, S.C., Boyd, O.S., Field, Ned, Chen, Rui,
1321 Rukstales, K.S., Luco, Nico, Wheeler, R.L., Williams, R.A., and Olsen, A.H., (2014).
1322 Documentation for the 2014 update of the United States national seismic hazard maps: U.S.
1323 Geological Survey Open-File Report 2014-1091, 243 p.
1324 <https://doi.org/10.3133/ofr20141091>.
- 1325 Petronis, M. S., Geissman, J. W., Oldow, J. S., & McIntosh, W. C. (2009). Late Miocene to
1326 Pliocene vertical-axis rotation attending development of the Silver Peak–Line Mountain
1327 displacement transfer zone, west-central Nevada. In J. S. Oldow, & P. H. Cashman (Eds.),
1328 Late Cenozoic Structure and Evolution of the Great Basin–Sierra Nevada Transition (pp.

- 1329 215–254). Colorado, USA, Special Paper 447: Geological Society of America.
- 1330 [https://doi.org/10.1130/2009.2447\(12\)](https://doi.org/10.1130/2009.2447(12)).
- 1331 Pierce, I. K. D., Wesnousky, S. G., Owen, L. A., Bormann, J. M., Li, X., & Caffee, M. (2021).
- 1332 Accommodation of plate motion in an incipient strike-slip system: The Central Walker Lane.
- 1333 *Tectonics*, 40, e2019TC005612. <https://doi.org/10.1029/2019TC005612>.
- 1334 Platt, J.P., and Becker, T. (2013). Kinematics of rotating panels of E–W faults in the San
- 1335 Andreas system: What can we tell from geodesy? *Geophys. J. Int.*, 194, 1295–1301.
- 1336 <https://doi.org/10.1093/gji/ggt189>.
- 1337 Pollitz, F.F., (1997). Gravitational-viscoelastic postseismic relaxation on a layered spherical
- 1338 Earth: *J. Geophys. Res.*, v. 102, p. 17,921– 17,941. <https://doi.org/10.1029/97JB01277>.
- 1339 Pollitz, F.F., (2022a). Viscoelastic fault-based model of crustal deformation for the 2023 update
- 1340 to the US National Seismic Hazard Model, *Seis. Res. Lett.* 93 (6), 3087–3099.
- 1341 <https://doi.org/10.1785/0220220137>.
- 1342 Pollitz, F.F., Evans, E.L., Field, E.H., Hatem, A.E., Hearn, E.H., Johnson, K., Murray, J.R.,
- 1343 Powers, P.N., Shen, Z.-K., Wespestad, C., Zeng, Y. (2022b). Western US deformation
- 1344 models for the 2023 update to the US National Seismic Hazard Model, *Seis. Res. Lett.* 93 (6),
- 1345 3068–3086. <https://doi.org/10.1785/0220220143>.
- 1346 Sandwell, D. T., Zeng, Y., Shen, Z.-K., Crowell, B., Murray, J., McCaffrey, R., & Xu, X. (2016).
- 1347 "The SCEC Community Geodetic Model V1: Horizontal Velocity Grid".
- 1348 https://topex.ucsd.edu/CGM/technical_report/CGM_V1.pdf.
- 1349 Savage, J.C. and Burford, R.O. (1973). Geodetic determination of relative plate motion in
- 1350 Central California, *J. Geophys. Res.*, v. 78, n. 5. p. 832-845.

- 1351 Savage, J.C., Gan, W. and Svare, J. L. (2001). Strain accumulation and rotation in the eastern
1352 California shear zone, *J. Geophys. Res.*, 106, 21,995–22,007.
- 1353 Seitz, G., Kent, G., Driscoll, N., Dingler, J. (2016). Large earthquakes on the Incline Village
1354 Fault from onshore and offshore paleoseismology, Lake Tahoe, California-Nevada, Chapter
1355 43, Applied Geology in California, AEG Special Publication Number 26, R. Anderson, H.
1356 Ferriz eds.
- 1357 Shen, Z.-K., Jackson, D.D., Ge, B.X. (1996). Crustal deformation across and beyond the Los
1358 Angeles basin from geodetic measurements, *J. Geophys. Res.*, v101, n. B12, p 27,957-
1359 27,980.
- 1360 Shen, Z.-K., Jackson, D.D., Kagan, Y.Y. (2007). Implications of Geodetic strain rate for future
1361 earthquakes, with a five-year forecast of M5 earthquakes in southern California, *Seis. Res.*
1362 *Lett.*, 78(1). <https://doi.org/10.1785/gssrl.78.1.116>.
- 1363 Shen, Z.-K., King, R. W., Agnew, D. C., Wang, M., Herring, T. A., Dong, D. and Fang, P.
1364 (2011), A unified analysis of crustal motion in Southern California, 1970–2004: The SCEC
1365 crustal motion map, *J. Geophys. Res. - Solid Earth*, 116, B11402.
1366 <https://doi.org/10.1029/2011JB008549>.
- 1367 Shen, Z.-K., Wang, M., Zeng, Y., Wang, F. (2015). Optimal interpolation of spatially discretized
1368 Geodetic data, *Bull. Seis. Soc. Am.*, 105 (4): 2117–2127. <https://doi.org/10.1785/0120140247>.
- 1369 Shen, Z.-K., and Bird, P. (2022). NeoKinema deformation model for the 2023 update to the US
1370 National Seismic Hazard Model, *Seismol. Res. Lett.*, 93(6), 3037–3052.
1371 <https://doi.org/10.1785/0220220179>.
- 1372 Spinler, J. C., Bennett, R. A., Anderson, M. L., McGill, S. F., Hreinsdóttir, S. and McCallister,
1373 A. (2010). Present-day strain accumulation and slip rates associated with southern San

- 1374 Andreas and eastern California shear zone faults, *J. Geophys. Res.- Solid Earth*, 115,
1375 B11407. <https://doi.org/10.1029/2010JB007424>.
- 1376 Slemmons, D.B., Jones, A.E., and Gimlett, J.I. (1965). Catalog of Nevada earthquakes, 1852–
1377 1960: *Geol. Soc. Am. Bull.*, v. 55, p. 537–583.
- 1378 Spakman, W. & Nyst, M.C.J., (2002). Inversion of relative motion data for estimates of the
1379 velocity gradient field and fault slip, *Earth planet. Sci. Lett.*, 203, 577–591.
1380 [https://doi.org/10.1016/S0012-821X\(02\)00844-0](https://doi.org/10.1016/S0012-821X(02)00844-0).
- 1381 Stewart, J.H., (1988). Tectonics of the Walker Lane belt, western Great Basin: Mesozoic and
1382 Cenozoic deformation in a zone of shear, in Ernst, W. G., ed., Metamorphism and crustal
1383 evolution of the west- ern United States: Prentice Hall, Englewood Cliffs, New Jersey, p.
1384 681-713.
- 1385 Surpless, B., (2008). Modern strain localization in the central Walker Lane, western United
1386 States: Implications for the evolution of intraplate deformation in transtensional settings,
1387 *Tectonophysics* 457, 239–253. <https://doi.org/10.1016/j.tecto.2008.07.001>.
- 1388 Tape, C., Musé, P., Simons, M., Dong, D., Webb, R., (2009). Multiscale estimation of GPS
1389 velocity fields, *Geophys. J. Int.*, 179(2), 945–971. [https://doi.org/10.1111/j.1365-246X.2009.04337.x](https://doi.org/10.1111/j.1365-
1390 246X.2009.04337.x).
- 1391 Thatcher, W., Foulger, G., Julian, B., Svarc, J., Quility, E., Bawden, G. (1999). Present-day
1392 deformation across the Basin and Range Province, western U.S. *Science*, 283(5408), 1714–
1393 1718. <https://doi.org/10.1126/science.283.5408.1714>.
- 1394 Unruh, J., Humphrey, J., Barron, A. (2003). Transtensional model for the Sierra Nevada frontal
1395 fault system, eastern California, *Geology*, v. 31, n. 4, p. 327–330.

- 1396 Unruh, J., Hauksson, E., Jones, C.H. (2014). Internal deformation of the southern Sierra Nevada
1397 microplate associated with foundering lower lithosphere, California *Geosphere*, v. 10, no. 1,
1398 p. 107–128. <https://doi.org/10.1130/GES00936.1>.
- 1399 Unruh, J. and Humphrey, J. (2017). Seismogenic deformation between the Sierran microplate
1400 and Oregon Coast block, California, USA, *Geology*, v. 45, n. 5, p. 415–418.
1401 <https://doi.org/10.1130/G38696.1>.
- 1402 U.S. Geological Survey and Nevada Bureau of Mines and Geology, Quaternary Fault and Fold
1403 Database for the United States, accessed April, 2011, at: <https://www.usgs.gov/natural->
1404 hazards/earthquake-hazards/faults.
- 1405 U.S. Geological Survey and California Geological Survey, Quaternary Fault and Fold Database
1406 for the United States, accessed April, 2011, at: <https://www.usgs.gov/natural->
1407 hazards/earthquake-hazards/faults.
- 1408 U.S. Geological Survey and Utah Geological Survey, Quaternary Fault and Fold Database for the
1409 United States, accessed April, 2011, at: <https://www.usgs.gov/natural-hazards/earthquake->
1410 hazards/faults.
- 1411 U.S. Geological Survey and Arizona Geological Survey, Quaternary Fault and Fold Database for
1412 the United States, accessed April, 2011, at: <https://www.usgs.gov/natural->
1413 hazards/earthquake-hazards/faults.
- 1414 Wallace, R.E., (1984). Patterns and timing of Late Quaternary faulting in the Great Basin
1415 Province and relation to some regional tectonic features, *J. Geophys. Res.*, v. 89, n. B7, p.
1416 5763-5769.
- 1417 Ward, S.N. (1998). On the consistency of earthquake moment rates, geological fault data, and
1418 space geodetic strain: the United States. *Geophys. J. Int.* 134, 172-186.

- 1419 Weldon, R.J., Humphreys, E.D., (1986). A kinematic model of Southern California, *Tectonics*,
1420 5(1), p. 33-48, ST0745.
- 1421 Wesnousky, S. G. (2005). Active faulting in the Walker Lane. *Tectonics*, 24, TC3009.
1422 <https://doi.org/10.1029/2004TC001645>.
- 1423 Wesnousky, S.G., Bormann, J.M., Kreemer, C., Hammond, W.C. and Brune, J.N. (2012).
1424 Neotectonics, geodesy, seismic hazard in the northern Walker Lane of western North
1425 America: Thirty kilometers of crustal shear and no strike-slip? *Earth and Planetary Science
Letters*, 329-330. <https://doi.org/10.1016/j.epsl.2012.02.018>.
- 1427 Wessel, P., Smith, W. H. F., Scharroo, R., Luis, J. and Wobbe, F. (2013). Generic Mapping
1428 Tools: Improved Version Released, *EOS Trans. AGU*, 94(45), p. 409-410.
1429 <https://doi.org/10.1002/2013EO450001>.
- 1430 Wicks, C. W., Thatcher, W., Monastero, F.C., Hasting, M.A. (2001). Steady state deformation of
1431 the Coso Range, east central California, inferred from satellite radar interferometry, *J.
1432 Geophys. Res.*, v. 106, n. B7, p. 13,769-13,780.
- 1433 Wilcox, R. R. (2005). Introduction to robust estimation and hypothesis testing, Elsevier
1434 Academic Press, Burlington, Mass.
- 1435 Williams, T. B., Kelsey, H. M., and Freymueller, J. T. (2006). GPS-derived strain in
1436 northwestern California and convergence of the Sierra Nevada–Great Valley block contribute
1437 to southern Cascadia forearc contraction: *Tectonophysics*, v. 413, p. 171–184.
1438 <https://doi.org/10.1016/j.tecto.2005.10.047>.
- 1439 Young, Z., Kreemer, C., Hammond, W.C. and Blewitt, G. (2023). Interseismic strain
1440 accumulation between the Colorado Plateau and the Eastern California Shear Zone:

- 1441 Implications for the seismic hazard near Las Vegas, Nevada, *Bull. Seis. Soc. Am.*, 113(2),
- 1442 856–876. <https://doi.org/10.1785/0120220136>.
- 1443 Zeng, Y. (2022a). A fault-based crustal deformation model with deep driven dislocation sources
- 1444 for the 2023 Update to the US National Seismic Hazard Model, *Seismo. Res. Lett.*, 93 (6),
- 1445 3170–3185. <https://doi.org/10.1785/0220220209>.
- 1446 Zeng, Y. (2022b). GPS velocity field of the western United States for the 2023 National Seismic
- 1447 Hazard Model update, *Seismol. Res. Lett.* 93, 3121–3134.
- 1448 <https://doi.org/10.1785/0220220180>.

Supporting Information for

**Robust Imaging of Fault Slip Rates in the Walker Lane and Western Great Basin
from GPS Data Using a Multi-Block Approach**

William C. Hammond¹, Corné Kreemer^{1,2}, Geoffrey Blewitt¹

1) Nevada Geodetic Laboratory,
Nevada Bureau of Mines and Geology,
University of Nevada, Reno,
Reno NV 89557

2) Nevada Seismological Laboratory,
University of Nevada, Reno,
Reno NV 89557

Contents of this file:

Supplemental Text
Supplemental Figures S1, S2, S3, S4, S5, S6, S7, S8

Additional Supporting Information (Files uploaded separately)

Supplemental Table S1. GPS velocities from combined continuous, semi-continuous and campaign velocities. Columns are:

1. Latitude (degrees)
2. Longitude (degrees)
3. East velocity (mm/yr)
4. North velocity (mm/yr)
5. East velocity uncertainty (mm/yr)
6. North velocity uncertainty (mm/yr)
7. Source (continuous, MAGNET or campaign GPS station)
8. Station name (4-char ID)

Supplemental Table S2. Fault slip rates. No normal component parameter was included faults with dip=90°. Faults with rake = ±90° had dip slip component parameters that were damped towards zero. Columns are:

1. Fault ID
2. Number of strike slip rate segment estimates
3. Number of normal slip rate estimates
4. Strike slip rate (mm/yr)
5. Normal rate (mm/yr)
6. Strike slip rate uncertainty (mm/yr)
7. Normal rate uncertainty (mm/yr)
8. Fault Name

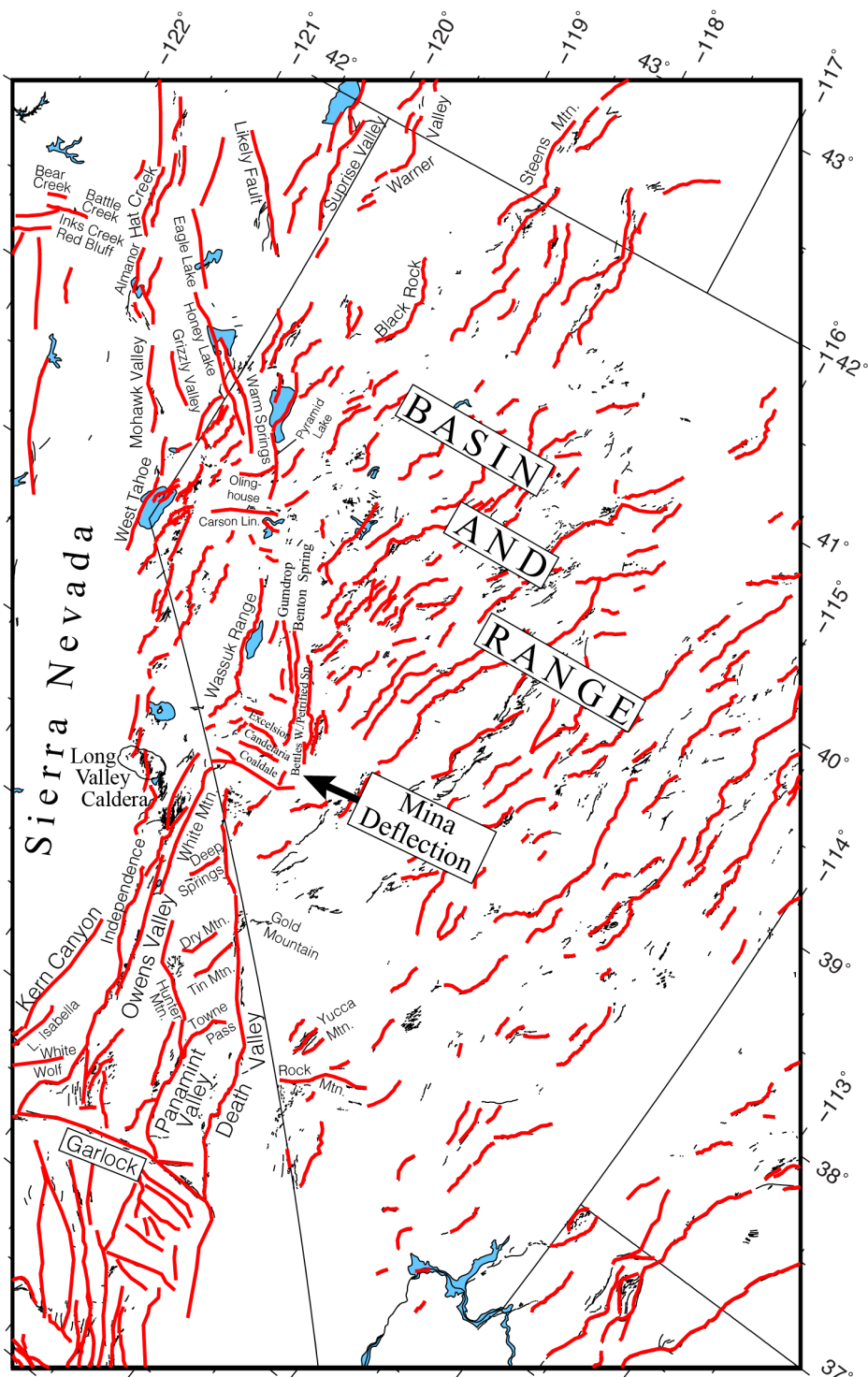


Figure S1. Faults in the NSHM database (red) (Hatem et al., 2022a), annotated with fault names for those mentioned in text. Additional faults from the Quaternary Fault and Fold Database (QFFD) are given with black line segments (USGS and NBMG, 2011; USGS and AGS, 2011; USGS and CGS, 2011; USGS and UGS, 2011).

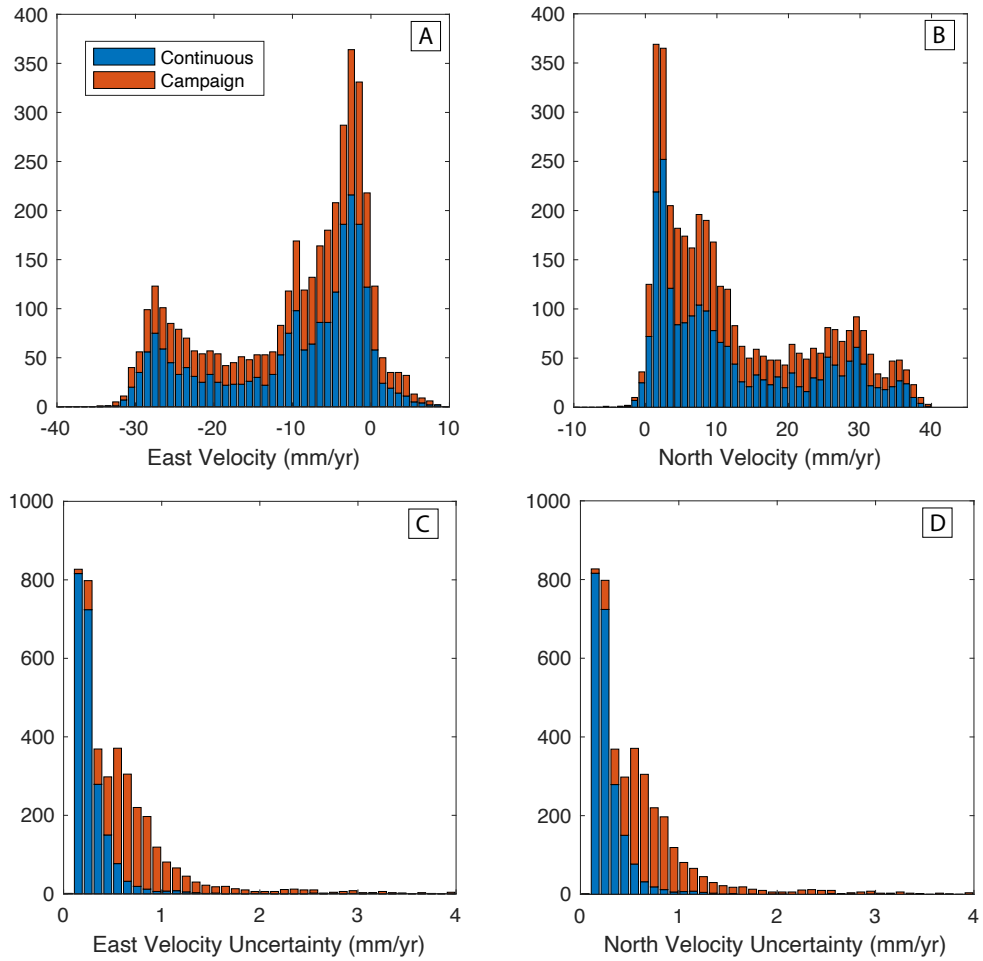


Figure S2. Histograms of A) east velocity, B) north velocity, C) east velocity uncertainty, D) north velocity uncertainty for stations inside the model domain shown in Figures 1 and S1. The red bars (campaign stations) sit on top of the blue bars (continuous stations) and show no systematic bias between campaign and continuous velocity fields. Campaign uncertainties are approximately twice those of continuous stations but are occasionally much larger.

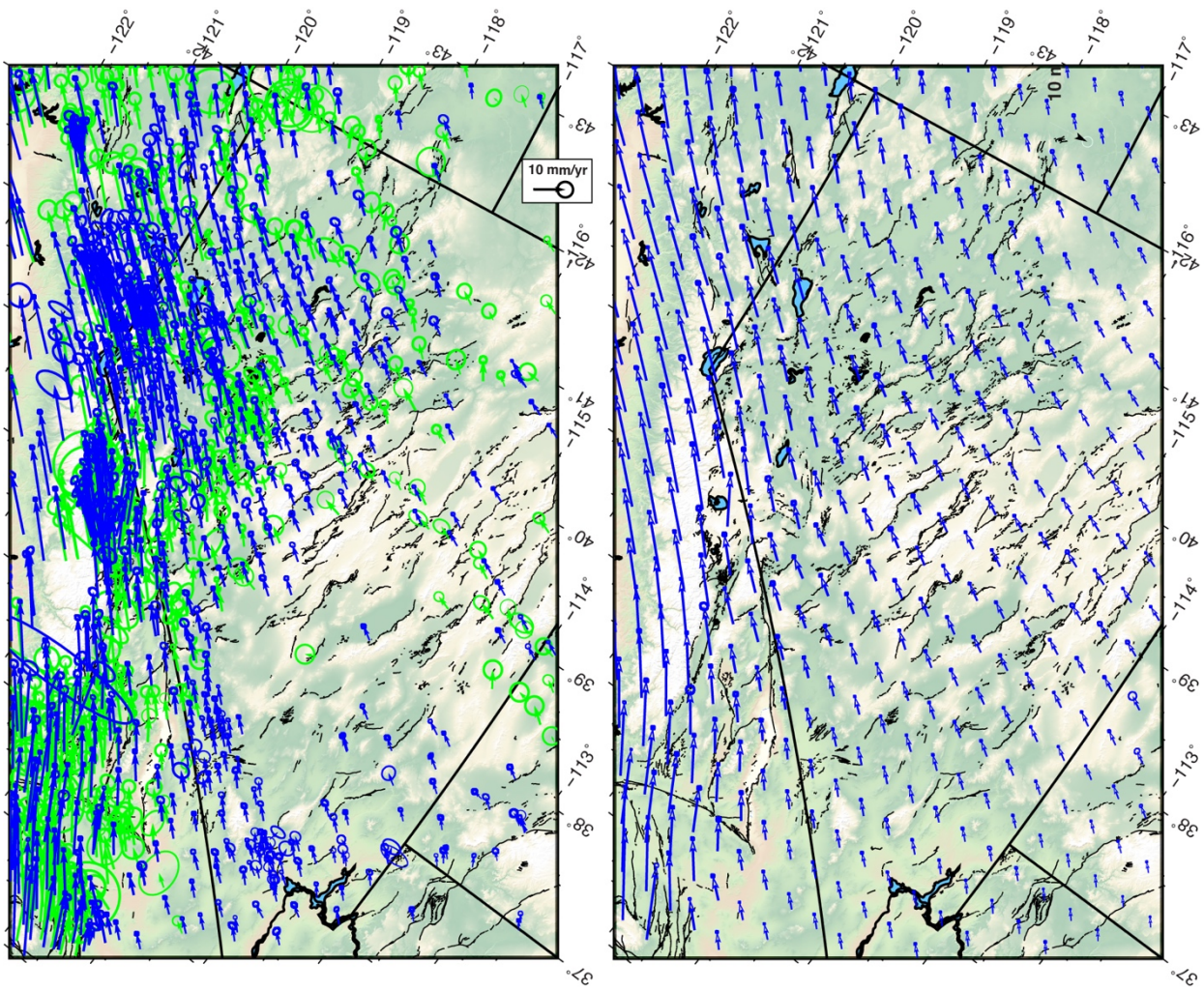


Figure S3. A) Campaign (green) and continuous (blue) velocities with error ellipses. B) Gridded horizontal GPS velocity vectors. The gridded field has been decimated to increase clarity of the figure. Actual grid spacing is $0.045^{\circ} \times 0.045^{\circ}$ ($\sim 5 \text{ km}$).

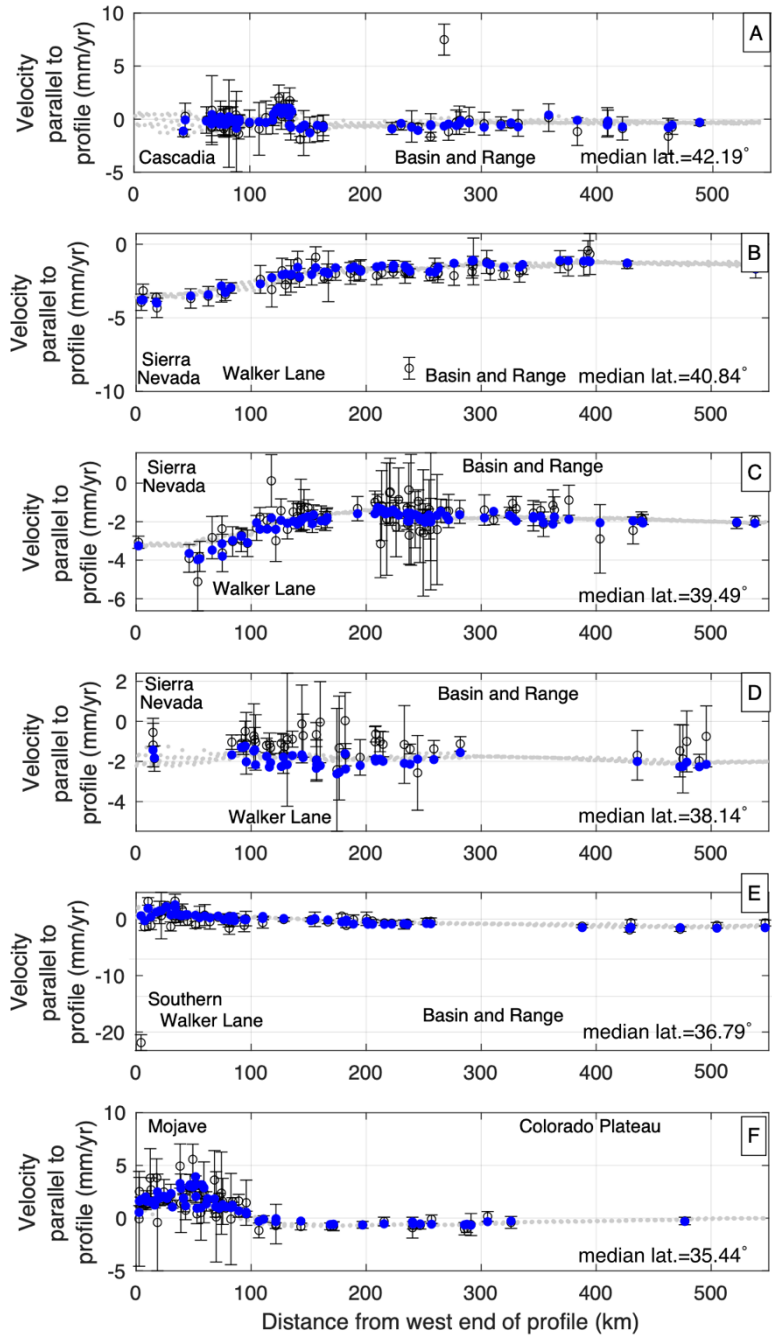


Figure S4. Profiles of GPS velocity component parallel to the lines shown in Figure 1A. Positive direction of profile is towards northeast end of line. Error bars on observed GPS velocities (black circles) are 2σ . Median spatial filtered GPS velocities (larger blue dots) are plotted on top of the gridded version of the velocity field (smaller gray dots). Faster profile-parallel motion on the west end of profiles E) and F) does not imply net contraction within the profile since they are not aligned with the direction of maximum extension.

Supplemental Text: Model Regularization

Strain Rates

In the strain rate mapping shown in Figure 3 we estimate the strain rate at each grid point in the map using gridded velocity data within a preselected horizontal distance from the point. The choice of distance is a horizontal length scale over which velocities gradients are estimated, and which adjusts the balance between strain rate model resolution and data fit. For example, choosing a very large length scale will use more data and give lower uncertainties in each estimate. However, there will be greater misfit to the data than a shorter length scale model since it is less able to explain horizontal variations in velocity gradients. Thus, we seek a length scale that finds a balance between having fine enough resolution to represent Walker Lane deformation patterns but also low uncertainty in the fit to the GPS data.

We test a sequence of length scales between 2 and 20 km. For each length scale we solve for a strain rate model and compute the model norm and misfit. Model norm is defined as the root sum square of all strain rate magnitudes, and the misfit is defined as the mean or median of χ^2 per degree of freedom (v) of all strain rate values in each strain rate map. Figure S5 shows that the model norms decrease, and the misfits increase with increasing averaging length scale. For the strain rate map shown in Figure 3 and for regularizing the block modeling analysis (see next section below) we choose a length scale of 8 km. This length scale has a relatively low misfit to the data, has significant structure in the model (high enough norm), and results in a strain rate model with enough detail to compare it to the distribution and patterns of faulting in the Walker Lane and Western Great Basin (Figure 3).

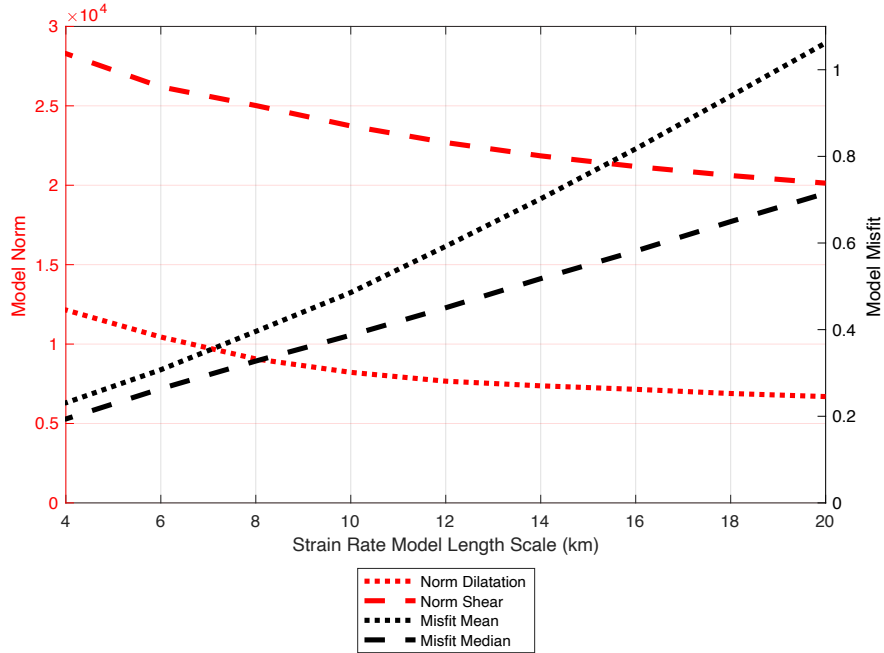


Figure S5. Model norm and misfit to GPS data as a function of assumed strain rate map horizontal length scale. Shear and dilatational strain rates (red dashed and dotted respectively) are shown separately, emphasizing that shear strain rates are much greater than dilatational strain rates in the Walker Lane, but both decrease with increasing length scale. Model median and mean misfit (black dashed and dotted respectively) are shown separately. Mean misfit tends to be greater than the median because it is more sensitive to relatively few but greater strain rates that are concentrated in narrow zones.

Slip Rates and Vertical Axis Rotation Rates

Like many geophysical inverse problems block models have parameters that are mixed determined in the sense that some parameters (in our case block rotations and slip rates) are well resolved by the data while others are not. Here the velocity field has been gridded which reduces the problem of uneven GPS data coverage. However, uncertainties in the velocity field still vary from location to location, block size and fault density also vary, which impacts uncertainty and covariance of model parameters.

In this study we use a geographically variable regularization for damping on slip rates (γ) and vertical axis spin rates (β), unlike Hammond et al., (2011) which used a geographically constant value. Because strain rates vary by orders of magnitude from one part of our model domain to the other it is reasonable to expect that the model parameters that represent fault slip do as well. To balance the inversion we regularize the parameters in such a way that they are proportional to the background strain rates (Figure 3). We introduce two parameters that are constant scale factors between the strain rates and slip rate damping regularization. The parameter φ_{shear} is the ratio between the shear strain rate and damping of the strike slip rates, while the parameter $\varphi_{dilatation}$ is the ratio between the dilatational strain rate and damping of the normal slip rates (horizontal extension component).

We find suitable values for φ_{shear} and $\varphi_{dilatation}$ by performing a grid search for a generated block model at a representative region with a center at -118° longitude and 36.5° latitude (Figures S6, S7, and S8). Values of both parameters are varied from 10^{-3} to 10^3 mm/ 10^{-9} in \log_{10} steps of 0.5. For each pair of values, we assign the damping on fault slip rates as

$$\gamma_{strike\ slip} = \varphi_{shear} \dot{\epsilon}_{shear} \quad S1)$$

$$\gamma_{horizontal\ extension} = \varphi_{dilatation} \dot{\epsilon}_{dilatation} \quad S2)$$

where $\dot{\epsilon}_{shear}$ and $\dot{\epsilon}_{dilatation}$ are the shear and dilatational components in the strain rate map at the mid-point of the fault. From each model we calculate norms of the strike slip rate, normal slip rate, and vertical axis spin rates. Predictions of each model are used to calculate misfit to the data. Figure S6 shows that model parameter norms are sensitive to φ_{shear} and $\varphi_{dilatation}$ and illustrates how changes in these parameters effect block system spin rates and slip rates. Using Figure S6 we select a point in the parameter space that is 1) near the lowest data misfit, 2) between the areas with the lowest and highest slip rate norms, and 3) near the domain with the lowest spin rate norms ($\varphi_{shear} = 1$ mm/ 10^{-9} and $\varphi_{dilatation} = 1$ mm/ 10^{-9}). The model obtained using the selected parameters has relatively low noise in the rotations and slip rates.

Damping of vertical axis spin rates β of each block is also applied. Damping of the vertical axis spin rates does not damp the translation component of the block motion which is well constrained by the GPS data. Instead, it damps only the vertical axis spin component which is the dot product between each block's overall Euler pole of rotation and the unit vector pointing from Earth center towards the centroid of the block on Earth's surface. We begin with a value of $\beta=10^{-9}$, slightly lower than the geographically constant value use by Hammond et al., (2011) for the Northern Walker Lane (they used $3.2e-9$). We start with a lower value because the algorithmically generated block sizes are smaller on average and have greater freedom to spin around vertical axes before violating the data. Also areas with higher strain rates tend to have

higher vorticity in the GPS velocity field so stronger spin rate damping is needed to prevent block spin rates from becoming unrealistically large. For areas with maximum shear strain rate $>100 \times 10^{-9}/\text{yr}$ we linearly decrease β until it reaches a minimum of $\beta = 10^{-11}$ in areas with strain rate greater than $200 \times 10^{-9}/\text{yr}$. This effects only a small area close to the San Andreas Fault system, at the southern end of our modeling domain because most shear strain rates in Walker Lane are less than $80 \times 10^{-9}/\text{yr}$ (Figure 3).

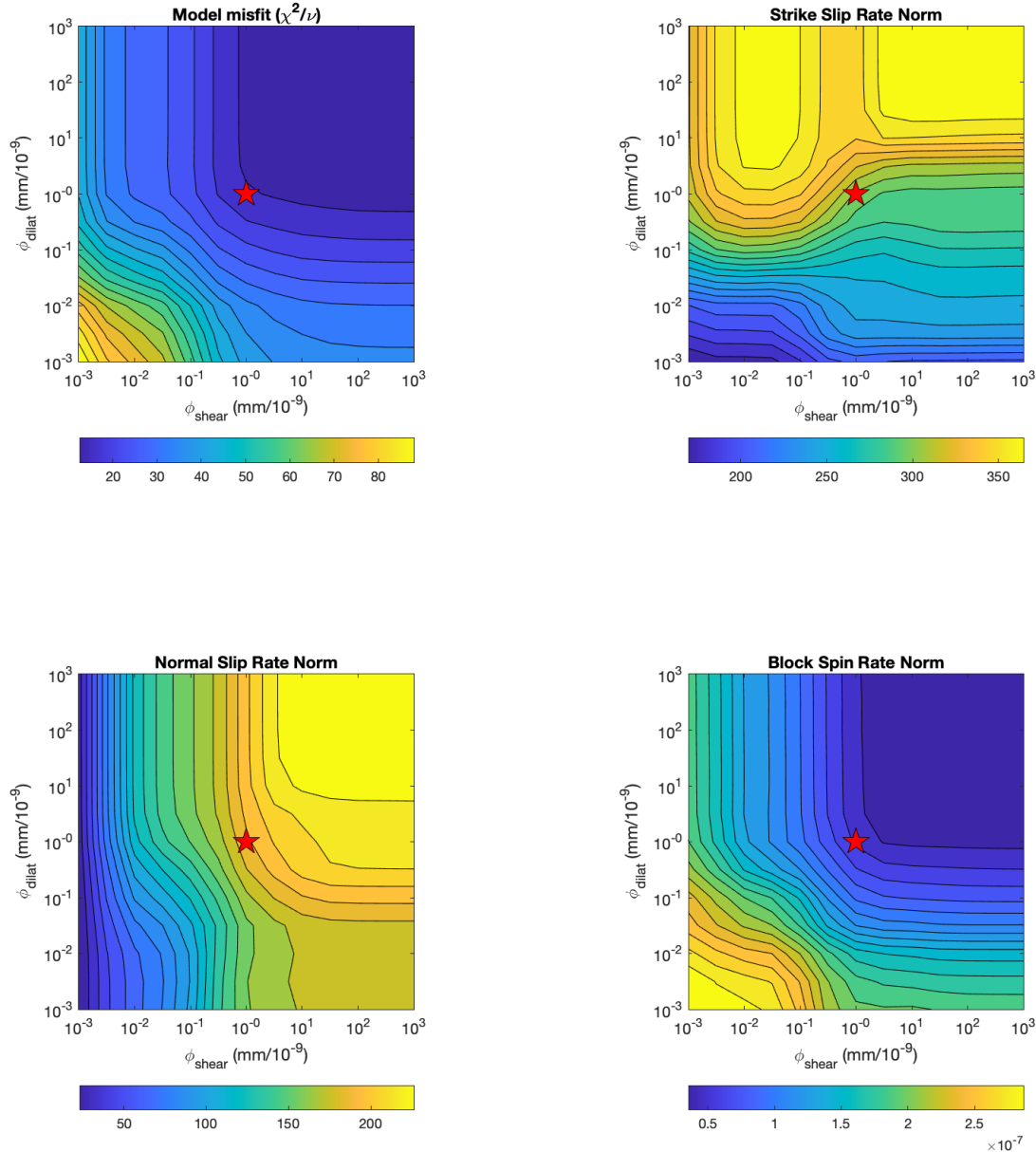


Figure S6. Results of grid search used to determine values for ϕ_{shear} and $\phi_{\text{dilatation}}$. Red star indicates location in parameter space of choice used in the solution. This choice of values strikes a balance between the need for low model misfit to the GPS data and model norm that is large enough for spin rates and slip rates.

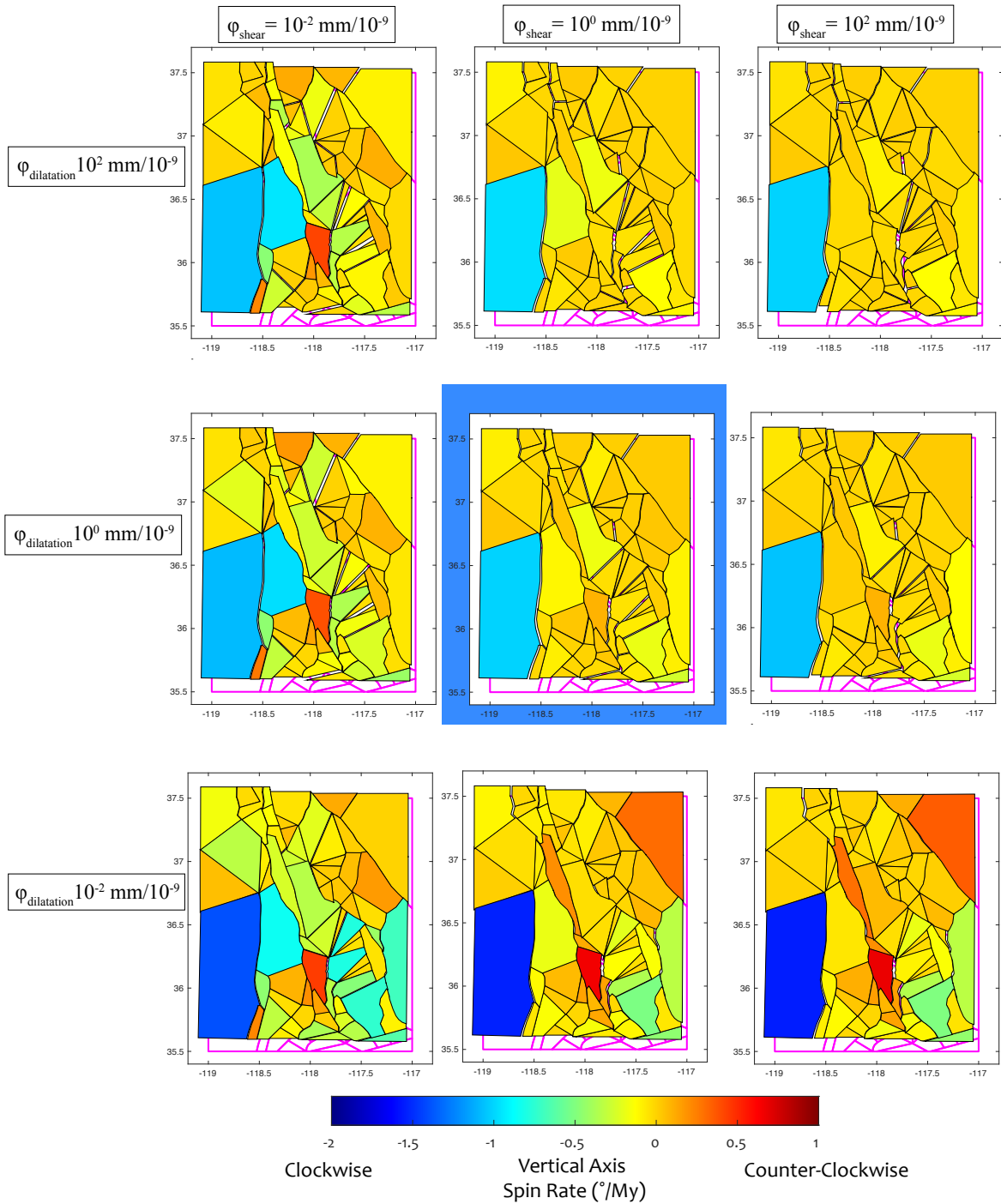


Figure S7. Examples of block models solved with various values for regularization parameters $\varphi_{\text{dilatation}}$ and φ_{shear} as indicated on the figure. Color scale indicates vertical axis spin rate in degrees per million years. Model in center with blue background is the one based on values found using Figure S6.

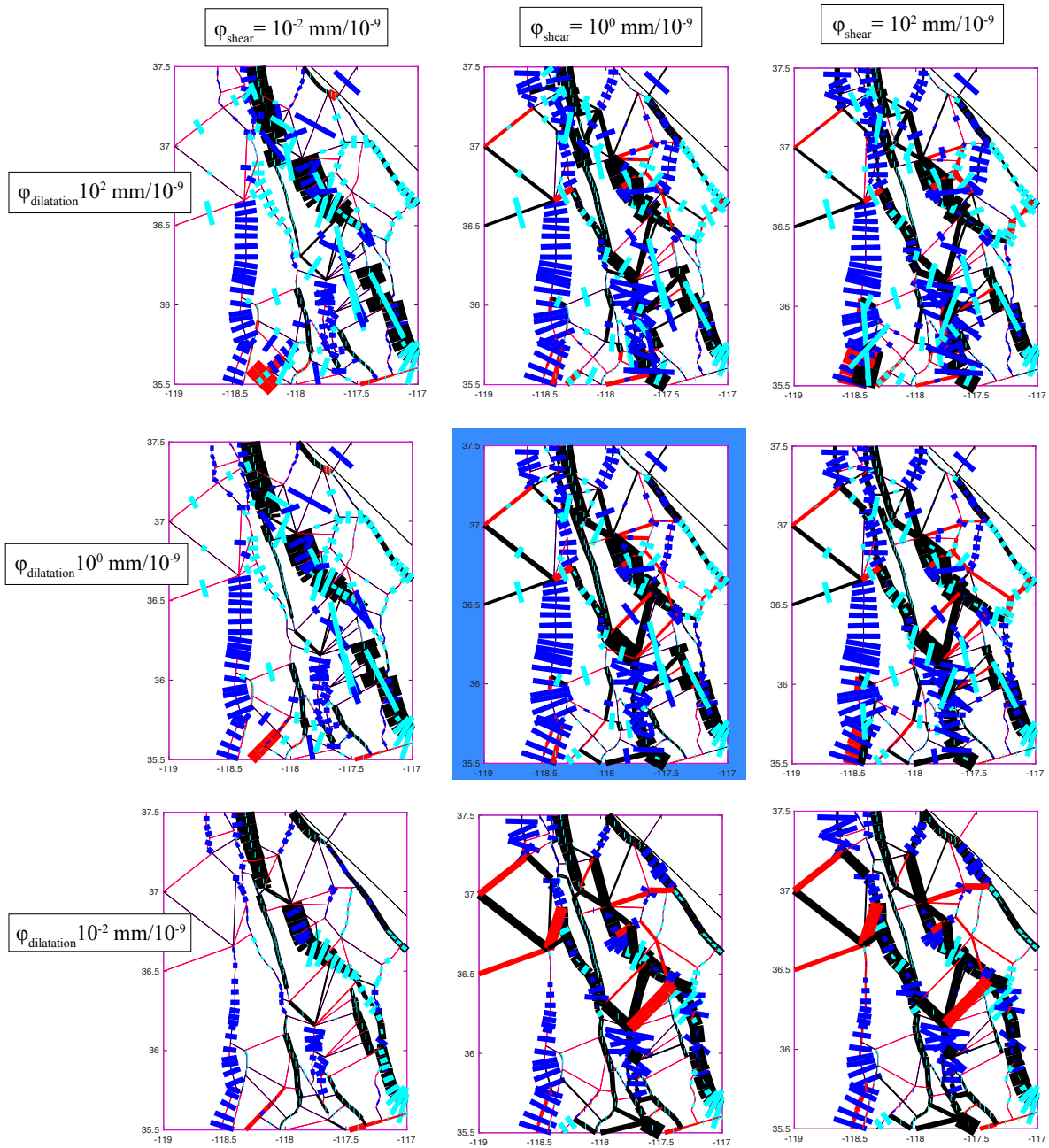


Figure S8. Slip rates associated with the same models as shown in Figures S6.

References for Supplemental Materials

Hammond, W. C., G. Blewitt, and C. Kreemer (2011), Block modeling of crustal deformation of the northern Walker Lane and Basin and Range from GPS velocities, *J. Geophys. Res.*, **116**, B04402, doi:10.1029/2010JB007817.

- Hatem, A.E., Collett, C.M., Briggs, R.W., Gold, R.D., Angster, S.J., Powers, P.M., Field, E.H., Anderson, M., Ben-Horin, J.Y., Dawson, T., DeLong, S., DuRoss, C., Thompson Jobe, J., Kleber, E., Knudsen, K.L., Koehler, R., Koning, D., Lifton, Z., Madin, I., Mauch, J., Morgan, M., Pearthree, P., Pollitz, F., Scharer, K., Sherrod, B., Stickney, M., Wittke, S., and Zachariasen, J., (2022a). Earthquake geology inputs for the U.S. National Seismic Hazard Model (NSHM) 2023 (western US) (ver. 2.0, February 2022): U.S. Geological Survey data release. <https://doi.org/10.5066/P9AU713N>.
- U.S. Geological Survey and Nevada Bureau of Mines and Geology, Quaternary Fault and Fold Database for the United States, accessed April, 2011, at: <https://www.usgs.gov/natural-hazards/earthquake-hazards/faults>.
- U.S. Geological Survey and California Geological Survey, Quaternary Fault and Fold Database for the United States, accessed April, 2011, at: <https://www.usgs.gov/natural-hazards/earthquake-hazards/faults>.
- U.S. Geological Survey and Utah Geological Survey, Quaternary Fault and Fold Database for the United States, accessed April, 2011, at: <https://www.usgs.gov/natural-hazards/earthquake-hazards/faults>.
- U.S. Geological Survey and Arizona Geological Survey, Quaternary Fault and Fold Database for the United States, accessed April, 2011, at: <https://www.usgs.gov/natural-hazards/earthquake-hazards/faults>.